Parameterization of oceanic whitecap fraction based on satellite observations

M. F. M. A. Albert[1], M. D. Anguelova[2], A. M. M. Manders[1], M. Schaap[1], and G. de Leeuw[1,3,4]

[1]{TNO, P.O. Box 80015, 3508 TA Utrecht, The Netherlands}

[2]{Remote Sensing Division, Naval Research Laboratory, Washington, DC 20375}

[3]{Climate Research Unit, Finnish Meteorological Institute, Helsinki, Finland}

[4]{Department of Physics, University of Helsinki, Helsinki, Finland}

Correspondence to: M. D. Anguelova (maggie.anguelova@nrl.navy.mil) and M. F. M. A. Albert (mfmaalbert@gmail.com)

Abstract

In this study the utility of satellite-based whitecap fraction (W) data for the prediction of sea spray aerosol (SSA) emission rates is explored. More specifically, the study is aimed at evaluating how an account for natural variability of whitecaps in the W parameterization would affect SSA mass flux predictions when using a sea spray source function (SSSF) based on the discrete whitecap method. The starting point is a data set containing W data for 2006 together with matching wind speed U_{10}, sea surface temperature (SST) T, and statistical data. Whitecap fraction W was estimated from observations of the ocean surface brightness temperature T_B by satellite-borne radiometers at two frequencies (10 and 37 GHz). A global scale assessment of the data set revealed a quadratic correlation between W and U_{10}. A new global $W(U_{10})$ parameterization was developed and used to evaluate an intrinsic correlation between W and U_{10} that could have been introduced while estimating W from T_B. A regional scale analysis over different seasons indicated significant differences of the coefficients of regional $W(U_{10})$ relationships. The effect of SST on W is explicitly accounted for in a new $W(U_{10}, T)$ parameterization. The analysis of W values obtained with the new $W(U_{10})$ and $W(U_{10}, T)$ parameterizations indicates that the influence of secondary factors on W is for the

largest part embedded in the exponent of the wind speed dependence. In addition, the $W(U_{10}, T)$ parameterization is capable to partially model the spread (or variability) of the satellite-based W data. The satellite-based parameterization $W(U_{10}, T)$ was applied in an SSSF to estimate the global SSA emission rate. The thus obtained SSA production rate for 2006 of 4.4×10^{12} kg yr^{-1} is within previously reported estimates, however with distinctly different spatial distribution.

1 Introduction

Whitecaps are the surface phenomenon of bubbles near the ocean surface. They form at wind speeds of around 3 m s^{-1} and higher, when waves break and entrain air in the water which subsequently breaks up into bubbles which rise to the surface (Thorpe, 1982; Monahan and Ó'Muircheartaigh, 1986). The estimated global average of whitecap cover, i.e., the fraction of the ocean surface covered with whitecaps W, is 2 to 5% (Blanchard, 1963). Being visibly distinguishable from the rough sea surface, whitecaps are the most direct way to parameterize the enhancement of many air-sea exchange processes including gas- and heat transfer (Andreas, 1992; Fairall et al., 1994; Woolf, 1997; Wanninkhof et al., 2009), wave energy dissipation (Melville, 1996; Hanson and Phillips, 1999), and the production rate of sea spray aerosols (SSA) (e.g., Blanchard, 1963; 1983; Monahan et al., 1983; O'Dowd and de Leeuw, 2007, de Leeuw et al., 2011), because all these processes involve wave breaking and bubbles.

Measurements of the whitecap fraction W are usually extracted from photographs and video images collected from ships, towers, and air planes (Monahan, 1971; Asher and Wanninkhof, 1998; Callaghan and White, 2009; Kleiss and Melville, 2011). Whitecap fraction is commonly parameterized in terms of wind speed at a reference height of 10 m, U_{10}. Wind speed is the primary driving force for the formation and variability of W (Monahan and Ó'Muircheartaigh, 1986; Salisbury et al., 2013, hereafter SAL13). Whitecap fractions predicted with conventional $W(U_{10})$ parameterizations show a large spread between reported W values (Lewis and Schwartz, 2004; Anguelova and Webster, 2006). Part of these variations is due to differences in methods of extracting W from still and video images. Indeed, the spread of W data has decreased in recently published in situ data sets as image processing improved and data volume increased (de Leeuw et al., 2011). However, an order-of-magnitude scatter of W data remains, suggesting that U_{10} alone cannot fully predict the W

variability. Other factors such as atmospheric stability (often expressed in terms of air-sea temperature difference), sea surface temperature (SST) T or friction velocity (combining wind speed and thermal stability (e.g., Wu, 1988; Stramska and Petelski, 2003)) have been indicated to affect W with implications for the SSA production. Thus, parameterizations of W that use different, or include additional (secondary), forcing parameters to better account for W variability have been sought (Monahan and Ó'Muircheartaigh, 1986; Zhao and Toba, 2001; Goddijn-Murphy et al., 2011; Norris et al., 2013b; Ovadnevaite et al., 2014; Savelyev et al., 2014).

An alternative approach to address the variability of W is to use whitecap fraction estimates from satellite-based observations of the sea state, because such observations provide long-term global data sets which encompass a wide range of meteorological and environmental conditions, as opposed to local measurement campaigns during which a limited variation of conditions is usually encountered. Brightness temperature T_B of the ocean surface measured from satellite-based radiometers at microwave frequencies has been successfully used to retrieve geophysical variables, including wind speed (Wentz, 1997; Bettenhausen et al., 2006; Meissner and Wentz, 2012). The feasibility of estimating W from T_B has also been demonstrated (Wentz, 1983; Pandey and Kakar, 1982; Anguelova and Webster, 2006). Anguelova et al. (2006; 2009) used WindSat data (Gaiser et al., 2004) to further develop the method of estimating W from T_B, and compiled a database of satellite-based W accompanied with additional variables. Figure 1a shows an example of the global W distribution from WindSat for a randomly chosen day.

Salisbury et al. (2013) showed that satellite-based W values carry a wealth of information on the variability of W. In particular, these authors showed that the global distribution of satellite-based W values differs from that obtained using a conventional $W(U_{10})$ parameterization with important implications for modeling SSA production rate in global climate models (GCMs) and chemical transport models (CTMs) (Salisbury et al., 2014). Salisbury et al. (2013) proposed a new $W(U_{10})$ parameterization in power law form using satellite-based W data over the entire globe for a full year. They derived wind speed exponents which are approximately quadratic for different data sets:

$$W_{10} = 4.6\times10^{-3}\times U_{10}^{2.26}; \qquad 2 < U_{10} \le 20 \text{ m s}^{-1},$$
$$W_{37} = 3.97\times10^{-2}\times U_{10}^{1.59}; \qquad 2 < U_{10} \le 20 \text{ m s}^{-1}, \tag{1}$$

where W is expressed in % and the subscripts denote the T_B frequencies used to obtain W. These exponents are significantly different from the cubic and higher wind speed dependences proposed by Callaghan et al. (2008, hereafter CAL08):

$$W = 3.18\times10^{-3}(U_{10}-3.70)^3; \qquad 3.70 < U_{10} \le 11.25 \text{ m s}^{-1}$$
$$W = 4.82\times10^{-4}(U_{10}+1.98)^3; \qquad 9.25 < U_{10} \le 23.09 \text{ m s}^{-1} \qquad (2)$$

and Monahan and O'Muircheartaigh (1980, hereafter MOM80):

$$W(U_{10}) = 3.84\times10^{-4}U_{10}^{3.41} \qquad (3).$$

The MOM80 parameterization was derived on the basis of the data sets of Monahan (1971) and Toba and Chaen (1973). Most of the wind speed values from these two data sets are up to 12 m s^{-1} with only 9% of the data points for winds up to ~18 m s^{-1}. The range of SST is from 17 to 31 °C. Monahan and O'Muircheartaigh (1986) emphasized that this is a regionally specific function, but its widespread adoption in global models led to its application at wind speeds and SSTs well above its range of validity.

In this study we explore the utility of the satellite-based W data from a standpoint of predicting SSA production rate. Whitecaps are used as a proxy for the amount of bubbles at the ocean surface. When these bubbles burst, they generate sea spray droplets which in turn transform to SSA when they equilibrate with the surroundings (Blanchard, 1983). Bursting bubbles produce film and jet droplets, whereas at high wind speeds, exceeding about 9 m s^{-1}, additional sea spray is directly produced as droplets which are blown off the wave crests (Monahan et al., 1983). These spume droplets are larger than the bubble-mediated SSA droplets (Andreas, 1992). In this study we will focus on bubble-mediated production of sea spray.

Sea spray aerosols are important for the climate system because, due to the vast extent of the ocean, SSA are amongst the largest aerosol sources globally (de Leeuw et al., 2011). SSA particles contribute to the scattering of short-wave electromagnetic radiation and thus to their direct radiative effect on climate. Also, having high hygroscopicity, SSA particles are a source for the formation of cloud condensation nuclei (Ghan et al., 1998; O'Dowd et al., 1999) and as such influence cloud microphysical properties and thus exert indirect radiative effects on the climate system. While residing in the atmosphere, SSA provide surface and

volume for a range of multiphase and heterogeneous chemical processes (Andreae and Crutzen, 1997). Through such chemical processes, the SSA contribute to the production of inorganic reactive halogens (Cicerone, 1981; Graedel and Keene, 1996; Keene et al., 1999; Saiz-Lopez and von Glasow, 2012), participate in the production or destruction of surface ozone (Keene et al., 1990; Barrie et al., 1988; Koop et al., 2000), and provide a sink in the sulfur atmospheric cycle (Chameides and Stelson, 1992; Luria and Sievering, 1991; Sievering et al., 1992; 1995).

The modeling of all these processes in GCMs and CTMs starts with calculation of the production rate of SSA particles (termed also SSA production flux, SSA generation, or SSA emission). A sea spray source function (SSSF) is used to calculate SSA production flux—the number of SSA particles produced per unit of sea surface area per unit time. The most commonly used SSSF, proposed by Monahan et al. (1986, hereafter M86), estimates SSA emission by the indirect, bubble-mediated mechanism. Based on the discrete whitecap method, the SSSF of M86 is formulated in terms of $W(U_{10})$, as defined by MOM80 (Eq. (3)), whitecap decay timescale τ, and the aerosol productivity per unit whitecap dE/dr:

$$\frac{dF}{dr_{80}} = \frac{W(U_{10})}{\tau}\frac{dE}{dr_{80}} = 1.373 \cdot U_{10}^{3.41} \cdot r_{80}^{-3}(1 + 0.057 r_{80}^{1.05}) \times 10^{1.19e^{-B^2}}, \quad (4)$$

In Eq. (4), the timescale is a constant τ = 3.53 s, r_{80} is the droplet radius at a relative humidity of 80%, and the exponent B is defined as $B = (0.38 - \lg r_{80})/0.65$. The term dE/dr, associated with the sea spray size distribution, determines the shape of the SSSF (i.e., shape factor); the term W/τ is a scaling (or magnitude) factor as it links predetermined SSA production per unit whitecap area with the amount of whitecapping in different regions at different seasons. Refer to Lewis and Schwartz (2004), de Leeuw et al. (2011), and Callaghan (2013) for clear distinction of the discrete whitecap method from the continuous whitecap method.

Estimates of SSA production fluxes using the discrete whitecap method still vary widely (Lewis and Schwartz, 2004; de Leeuw et al., 2011) precluding reliable estimates of the direct and indirect effects by SSA in GCMs, as well as the outcome of heterogeneous chemical reactions taking place in and on SSA particles in CTMs. The wide spread of predicted SSA emissions is caused by a combination of uncertainties coming from both the magnitude and the shape factors of the used SSSFs. The uncertainties associated with the magnitude factor include difficulties of measuring W and τ and their natural variability, which

affects the $W(U_{10})$ parameterizations. The assumptions of the discrete whitecap method (detailed in Sect. 2.4) also contribute to the uncertainty. Added to these are the uncertainties associated with the shape factor, such as its natural variability and the model chosen to parameterize the SSA size distribution. A source of uncertainty is the difficulty of directly measuring SSA fluxes which are used to develop and/or constrain SSSFs. When measurements of SSA concentrations are used to develop an SSSF, uncertainty comes from the deposition velocity model used to convert the concentrations to fluxes (e.g., Smith et al., 1993; Savelyev et al., 2014).

Aside from addressing uncertainties due to measuring techniques, there are two possible ways to improve the performance of a whitecap-based SSSF as regards the physical processes involved. One way is to address variations and uncertainties in the size-resolved productivity dE/dr_{80} (i.e., the shape factor in the SSSF), for instance by including the organic matter contribution to SSA at sub-micron sizes (O'Dowd et al., 2004; Albert et al., 2012) and/or by accounting for its variations with environmental factors instead of keeping it constant for all conditions (de Leeuw et al., 2011, Norris et al., 2013a; Savelyev et al., 2014). Another way is to address the variations and uncertainties in the whitecap fraction W (i.e., the magnitude factor in the SSSF) by steady improvements of the W measurements and by accounting for its natural variability. Both approaches are expected to reduce, or at least to better account for, the variations and uncertainties in parameterizing SSA flux.

Here we report on a study investigating the second of these two routes, namely—how using W data, which carry information for secondary factors, would influence the SSA production flux. The objective is to assess how much of the uncertainty in the SSA flux can be explained with the natural variability of W. Our approach (Sect. 2) involves three steps. We first assess the satellite-based whitecap database to evaluate the wind speed dependence of W over as wide a range of U_{10} values as possible (sect. 3.1.1). In assessing the W database, we also evaluate the impact of an intrinsic correlation between W and U_{10}, which could have been introduced in the process of estimating W from T_B (SAL13) (Sect. 3.1.2). We next apply the established wind speed dependence to W on regional scales in order to gain insights into the influence of secondary factors in different locations during different seasons (Sect. 3.2). In this second step, we use the results of our regional analysis to derive a new W parameterization that incorporates the effect of sea surface temperature (SST) T on W. The new $W(U_{10}, T)$ parameterization is compared to those of MOM80, CAL08, and SAL13 (Sect.

3.3). The utility of the new $W(U_{10}, T)$ parameterization is evaluated by using it to estimate SSA emissions and comparing to previous predictions of SSA emissions (Sect. 3.4).

2 Methods

2.1 Approach to derive whitecap fraction parameterization

Reasoning on a series of questions shaped our approach to parameterizing W and justified the choices we made for its implementation (Sect. 2.3). We first considered, Why do we need to parameterize W instead of using satellite-based W data directly? A major benefit of using satellite-based W data directly in an SSSF is that these data reflect the amount and persistence of whitecaps as they are formed by both primary and secondary forcing factors acting at a given location. This approach limits the uncertainty to that of estimating W from satellite measurements and does not add uncertainty from deriving an expression for $W(U_{10})$ or $W(U_{10}, T,$ etc.). However, such an approach would limit global predictions of SSA emissions to monthly values because a satellite-based W data set does not provide daily global coverage; i.e., one would need data like that in Fig. 1a for at least two weeks (and more for good estimates of the uncertainties) in order to have full coverage of the globe.

Alternatively, a parameterization of whitecap fraction derived from satellite-based W data can provide daily estimates of SSA emissions using readily available daily data of wind speed and other variables. Importantly, such a parameterization will be globally applicable because the whitecap fraction data cover the full range of meteorological conditions encountered over most of the world oceans. Because the availability of a large number of W data would ensure low error in the derivations of the $W(U_{10})$ or $W(U_{10}, T,$ etc.) expressions, we proceed with deriving a parameterization for W using the data in the whitecap database (Sect. 2.2.1).

The next question to consider was, How to account for the influence of secondary factors? Generally, to fully account for the variability of whitecap fraction, a parameterization of W would involve wind speed and many additional forcings explicitly to derive an expression $W(U_{10}, T,$ etc.) (MOM80; Monahan and Ó'Muircheartaigh, 1986; Anguelova and Webster, 2006). The SAL13 analysis showed substantial variations of W as a function of different variables, including SST. Because SST and wind speed are readily available variables, it would be useful to start with parameterization $W(U_{10}, T)$.

The question that arises next is, How to combine the different dependences of W? One possibility is to use a single-variable regression to extract the W dependence on each variable separately, e.g., $W(U_{10})$ and $W(T)$. Then, these can be combined to derive an expression for their effects in concert, e.g., $W(U_{10}, T) = W(U_{10})W(T)$. While variables like T, atmospheric stability, surfactants, etc. influence W, they do not cause whitecapping. So a parameterization formulated with dedicated $W(T)$ and other expressions may put undue weight on such influences. This approach can be pursued when we have enough information to judge the relative importance of each influence (e.g., Anguelova et al., 2010, their Fig. 6) and include it in a combined expression with a respective weighting factor.

Previous experience points to another possibility to combine causal variables like U_{10} and influential variables like T and the likes. The Monahan and O'Muircheartaigh (1986) analysis of five data sets showed that the variability of W caused by SST (and the atmospheric stability) affect significantly the coefficients in the wind speed dependence $W(U_{10})$, especially the wind speed exponent. The survey of $W(U_{10})$ parameterizations by Anguelova and Webster (2006, their Tables 1 and 2) also clearly shows that each campaign conducted in different regions and conditions comes up with a specific wind speed exponent. This strongly suggests that the influence of secondary factors is expressed as a change of the wind speed exponent. On the basis of their principal component analysis, SAL13 also suggested that in describing the W variability, it is more effective to combine individual variables with wind speed. On this ground, we proceed to obtain $W(U_{10}, T)$ as a wind speed dependence $W(U_{10})$ whose regression (or parametric) coefficients vary with SST. This goal can be realized by first identifying a general wind speed dependence to use as a reference, then quantifying the variations of its regression coefficients in different regions and seasons.

The important question now is, What functional form should we use for the general (reference) $W(U_{10})$ dependence? Equations (1)-(3) exemplify the functional forms usually employed to express $W(U_{10})$:

$$W = aU_{10}^{n} \tag{5a}$$

$$W = a(U_{10} + b)^{3} \tag{5b}.$$

A general $W(U_{10})$ dependence derived using Eq. (5a) would provide an empirical wind speed exponent n determined from available data sets, as MOM80 did using the available data sets at the time (Sect. 1). The wider the range of conditions represented by the data sets is, the closer the resulting $W(U_{10})$ dependence would be to average conditions globally and seasonally.

A general $W(U_{10})$ dependence derived using Eq. (5b) would provide a physically-based wind speed exponent $n = 3$ consistent with dimensional (scaling) arguments. Namely, because W is related to the rate at which the wind supplies energy to the sea, W should be proportional to the cube of the friction velocity u_* (Monahan and O'Muircheartaigh, 1986; Wu, 1988). On this basis, Monahan and Lu (1990) related $W^{1/3}$ to U_{10} and derived the cubic power law in Eq. (5b). Subsequently, this relationship was used successfully in whitecap data analyses (e.g., Asher and Wanninkhof, 1998; CAL08). Coefficient b in Eq. (5b) is included because it is preferable for a $W(U_{10})$ relationship to involve a finite y-intercept (Monahan and O'Muircheartaigh, 1986). A negative y-intercept determines b from the x-intercept and is usually interpreted as the threshold wind speed for whitecap inception.

A modified version of Eq. (5) combines the merits of both formulations into the form:

$$W = a(U_{10} + b)^n \tag{6}$$

where the wind speed exponent is adjustable and a finite y-intercept is included. A general $W(U_{10})$ dependence derived using Eq. (6) would provide a wind speed exponent as dictated by the whitecap database that is applicable to all satellite-based W data. Being representative of globally averaged conditions, this general $W(U_{10})$ dependence can be applied with the same n to different regional scales and seasonal timeframes affording quantification of its variations with SST via coefficients a and b. Any of the three formulations (Eqs. (5 and 6)) can produce a viable general $W(U_{10})$ dependence, the empirical one representative of the average conditions of the world oceans and the physical one supported by sound reasoning.

2.2 Data sets

To implement the approach thus formulated, we use the whitecap database on a global scale for the general $W(U_{10})$ dependence, and regional W subsets extracted from the whitecap database for the SST analysis. In describing the data sets used, we start with the whitecap database (Sect. 2.2.1). The considerations given to extract regional data sets from it are described in Sect. 2.2.2. We also introduce the data from the European Centre for Medium range Weather Forecasting (ECMWF) used in this study as an independent source to investigate possible intrinsic correlation among the entries of the whitecap database (Sect. 2.2.3).

2.2.1 Whitecap database

Anguelova and Webster (2006) describe in detail the general concept of retrieving the whitecap fraction W from measurements of the brightness temperature T_B of the ocean surface with satellite-borne microwave radiometers. Salisbury et al. (2013) describe the basic points of the retrieval algorithm estimating W (hereafter referred to as the $W(T_B)$ algorithm). Briefly, the algorithm obtains W by using measured T_B data for the composite emissivity of the ocean surface and modelled T_B data for the emissivity of the rough sea surface and areas that are covered with foam (Bettenhausen et al., 2006; Anguelova and Gaiser, 2013). Minimization of the differences between the measured and modelled T_B data in the $W(T_B)$ algorithm ensures minimal dependence of the W estimates on model assumptions and input parameters. An atmospheric model is necessary to evaluate the contribution from the atmosphere to T_B.

Wind speed U_{10} is one of the required inputs to the atmospheric, roughness and foam models (Anguelova and Webster, 2006; Salisbury et al., 2013). Wind speed data come from the SeaWinds scatterometer on the QuikSCAT platform or from the Global Data Assimilation System (GDAS), whichever matches up better with the WindSat data in time and space within 25 km and 60 min; hereafter we refer to both QuikSCAT or GDAS wind speed values as U_{10} from QuikSCAT or $U_{10\mathrm{QSCAT}}$. The use of $U_{10\mathrm{QSCAT}}$ in the estimates of satellite-based W is anticipated to lead to some intrinsic correlation when/if a relationship between W and $U_{10\mathrm{QSCAT}}$ is sought.

The W data used in this study are obtained from T_B at 10 and 37 GHz, W_{10} and W_{37}; data for 37 GHz are shown in Fig. 1a. The W_{10} and W_{37} data approximately represent different stages of the whitecaps because of different sensitivity of microwave frequencies to foam

thickness (Anguelova and Gaiser, 2011). Data W_{10} are a upper limit for predominantly active wave breaking (stage A whitecaps (Monahan and Woolf, 1989)) partially mixed with decaying (stage B) whitecaps, while W_{37} data quantify both active and decaying whitecaps. Because decaying foam covers a much larger area of the ocean surface than active whitecaps (Monahan and Woolf, 1989), W_{37} data are larger than W_{10} data. Comparisons to historic and contemporary in situ W data in Fig. 1b confirm the approximate representations of stage A whitecaps (cyan squares) and A + B whitecaps (blue diamonds) by W_{10} (green) and W_{37} (magenta), respectively. Anguelova et al. (2009) have quantified the differences between satellite-based and in situ W data using both previously published measurements and time-space match-ups of W and discussed possible reasons for the discrepancies.

The satellite-based W data are gridded into a 0.5°×0.5° grid cell together with the variables accompanying each W data point, namely $U_{10QSCAT}$, T from GDAS, time (average of the times of all samples falling in each grid cell), and statistical data generated during the gridding including the root-mean-square (rms) error, standard deviation (SD), and count (the number of individual samples in a satellite footprint averaged to obtain the daily mean W for a grid cell). In this study, we used daily match-ups of W, U_{10}, and T data for each grid cell for the year 2006. Due to large data gaps in both space and time, the daily W data cannot be interpolated to provide better coverage (Fig. 1a). Therefore, only the available data are used without filling the gaps for areas where data are lacking. This global data set was used to assess the globally averaged wind speed dependence of W.

2.2.2 Regional data sets

The annual global W distributions show regions with valid data points ranging from 100 to 300 samples per grid cell per year when both ascending and descending satellite passes are considered. There are fewer samples for latitudes beyond 60°S or N (see Fig. 1a) because WindSat and QuikSCAT have fewer matching points there (Sect. 2.2.1). Thus, different regions were selected using two criteria, namely (i) consider regions with a high number of valid data points, and (ii) obtain a selection representative of different conditions in the northern and southern hemispheres (NH and SH).

With these criteria, 12 regions of interest were selected (Fig. 2) and W, U_{10}, and T data for each region were extracted from the whitecap database. The coordinates of the selected regions are listed in Table 1, together with the corresponding number of samples and

minimum, maximum, mean, and median values for wind speed and SST for January and July. For 90% of the regional and monthly data used in the study, the percent difference (PD, defined as the difference between two values divided by the average of the two values) between mean and median values of U_{10} and T is less than 4% and 9.5%, respectively. With medians and means approximately the same, the U_{10} and T data have normal distributions; i.e., outliers, though existing, do not affect the mean values significantly. All analyses presented here use the mean U_{10} and T values. Figure 3 shows the seasonal cycles of the mean U_{10} and T values for four of the selected 12 regions visualizing the full range of U_{10} and T data (Table 1).

Regions 2-11 are all in the open ocean, region 1 was selected for its landlocked position. Region 6 in the Pacific Doldrums is used as a reference for the lower limit of U_{10} (Fig. 3a), while region 12 is included to represent the lowest T values (Fig. 3b). Four regions (2, 3, 7, and 8) are at latitudes between 0 and 30°S and N (Tropics and Subtropics) representing the Trade winds zone with persistent (Easterly) winds blowing over approximately the same fetches (except region 8) in oceans with different salinity (Tang et al., 2014) and primary production (Falkowski et al., 1998) (a proxy for surfactant concentrations). Region 4 is in the NH temperate zone representing long-fetched Westerly winds. Region 5 covers the latitudes between 40°S and 50°S known as “The Roaring Forties” for the strong Westerly winds there, characterized with long fetch as well. Differences in the seasonal cycles of U_{10} and T in regions 4 and 5 (Fig. 3) suggest more uniform conditions and longer fetches in the SH temperate zone. We have chosen regions 8 and 9 to represent different zonal conditions and to gauge the effect of narrower range of SST variations (as compared to the SST range in region 5). Chosen at the same latitude, regions 9-11 have approximately the same SST, salinity, and surfactants but represent different wind fetches, shortest for region 9 and longest for region 11. Overall, the chosen regions cover the full range of global oceanic conditions and are representative of diverse regional conditions.

2.2.3 Independent data source

Ideally, when deriving a $W(U_{10})$ parameterization, the data for W and U_{10} should come from independent sources. The intrinsic correlation between W and U_{10} that might have arisen from the use of U_{10} from QuikSCAT in the estimates of W from T_B (Sect. 2.2.1), might affect the relationship between W and U_{10} developed here. To evaluate the magnitude of such intrinsic

correlation, we used U_{10} from the ECMWF ($U_{10ECMWF}$), which is considered to be a more independent source. Note though that even the ECMWF data are generated by assimilating observational data sets (e.g., from buoys) in a coupled atmosphere-wave model (Goddijn-Murphy et al., 2011).

To compile this "independent" data set, we made time-space matchups between the W_{10} and W_{37} data and $U_{10ECMWF}$. In this way, for each W–$U_{10QSCAT}$ pair from the original W database, we have a corresponding W–$U_{10ECMWF}$ pair of data. To speed up calculations, and because this already provides a statistically significant amount of data, we used only ascending satellite overpasses. Wind speeds above 35 m s^{-1} were discarded. Besides ECMWF wind data, for consistency we also extracted ECMWF SST values.

Figure 4a shows all ECMWF wind speed data that have been matched in time and space with the available $U_{10QSCAT}$ data for March 2006. The majority of the data is clustered in the range of 5-10 m s^{-1}. To characterize the difference between the two wind speed sources, the correlation between U_{10} from ECMWF and U_{10} from QuikSCAT was determined as the best linear fit forced through zero:

$$U_{10\ ECMWF} = 0.952\ U_{10\ QSCAT} \quad (7)$$

with $R^2 = 0.844$. For comparison, the unconstrained fit between $U_{10QSCAT}$ and $U_{10ECMWF}$ is also shown in Fig. 4a (dashed line); both fits are very close (they almost overlap) with almost identical correlation coefficients ($R^2 = 0.845$ for the unconstrained fit). Similarly, Fig. 4b compares T from ECMWF and GDAS showing almost 1:1 correlation. That is, the two data sources provide almost the same values for T.

On average, U_{10} from ECMWF is about 5% lower than U_{10} from QuikSCAT. This U_{10} difference can be explained to some extent with the effect of atmospheric stability because QuikSCAT provides equivalent neutral wind which accounts for the stability effects on the wind profile (Kara et al., 2008; Paget et al., 2015), while the ECMWF model gives stability dependent wind speeds (Chelton and Freilich, 2005).

Having the correlations between U_{10} and T from the whitecap database and ECMWF quantified, one can evaluate differences caused by the use of different data sources. Equation (7) could also be useful when one decides to use ECMWF data because of their availability at 6 or 3 h intervals as compared to the availability of W, U_{10}, and T match-ups twice a day (Sect. 2.2.1).

2.3 Implementation

We aim to develop an expression capable of modeling both the trend of W with U_{10} and the spread of the satellite-based W data (see green and magenta symbols in Fig. 1b). We analyze the global data set of satellite-based W_{10} and W_{37} data and derive a general $W(U_{10})$ expression that represents average wind conditions in different geographical environments (i.e., the trend of W with U_{10}). Following Monahan and Lu (1990), we derive an expression in the form of Eq. (6) by plotting $W^{1/n}$ as a function of $U_{10\mathrm{QSCAT}}$. Applying linear regression, we find an expression:

$$W^{1/n} = mU_{10} + c \tag{8}$$

which is then rearranged and raised to the power n providing coefficients $a = m^n$ and $b = c/m$ in Eq. (6) (results in Sect. 3.1.1). All linear fits are done on the W data points associated with U_{10} from 3 to 20 m s^{-1}. The lower limit of 3 m s^{-1} is chosen as a threshold for observing whitecaps. This restriction is reasonable in light of the SAL13 analysis in which W data with a relative standard deviation $(\sigma_W / W) > 2$ were removed. The discarded W data were about 10% of all W data, mostly in regions with low wind speeds of around 3 m s^{-1}. We exclude the high wind speed regime in order to avoid uncertainty due to (i) fewer data points in this regime; and (ii) anticipated larger uncertainty in the W data from the $W(T_B)$ algorithm. With the wind speed threshold imposed in this way, we propose a broader interpretation of regression coefficient b (sect. 3.1.1).

For the intrinsic correlation analysis, the W–$U_{10\mathrm{ECMWF}}$ data pairs are used in a similar fashion to make $W^{1/n}(U_{10\mathrm{ECMWF}})$ linear fits and derive from them a relationship between the satellite-based W data and the ECMWF wind speeds. The two global $W(U_{10})$ parameterizations for the two wind speed sources are then compared to evaluate the magnitude of the intrinsic correlation (results in Sect. 3.1.2).

Because Eq. (7) gives the possibility to evaluate discrepancies due to the use of different sources for U_{10} and T, we use U_{10} and T from the whitecap database in all subsequent analyses and results. In this way, with the intrinsic correlation characterized, we restrict the uncertainty in our analyses by using the close matching-up of W, U_{10}, and T data in the whitecap database. This decision is reasonable considering that both data sets can be used in practice for different applications. The collocated data in the whitecap database (involving

QuikSCAT) are most handy for analysis (as done in this study). Meanwhile, W data from the whitecap database combined with forcing data from a global model (such as ECMWF or other) are useful for forecasts and climate simulations.

With n for the general wind speed dependence determined, we then apply Eq. (6) with the same n to the regional monthly sub-sets of W_{10} and W_{37} data. All available data per month were used, ranging from 22 to 31 days of data. Once again, scatter plots of $W^{1/n}(U_{10})$ were generated and the best linear fits were determined providing coefficients m and c for each region for each month for W_{10} and W_{37}. The regional and seasonal variations of coefficients m and c, as well as a and b, are analyzed to judge to what extent these variations warrant parameterization in term of SST $a(T)$ and $b(T)$ (results in Sect. 3.2).

To quantify how $a(T)$ and $b(T)$ are influenced by the functional form of the general wind speed dependence—our empirically determined wind speed exponent n (Eq. (6)) and the physically reasoned cubic wind speed dependence (Eq. (5b))—we also analyzed scatter plots of $W^{1/3}(U_{10})$ and derived a respective set of coefficients $a(T)$ and $b(T)$.

We analyzed the variations of coefficients m and c with the Student's T-statistics and Analysis of variance (ANOVA) tests. The Student test verifies whether two data sets (or sample populations) have significantly different means by confirming or rejecting the null hypothesis (the default statement that there is no difference among data sets). A small significance value (e. g., $p < 0.05$) for any pair of regional m and c data sets would indicate that the regional means of coefficients m and c are significantly different. The ANOVA test essentially does the same but for a group of three or more data sets simultaneously. ANOVA rejects the null hypothesis if two or more populations differ with statistical significance. In this sense, an ANOVA test is less specific than a Student test. Because the ANOVA assumptions (that the data sets are normally distributed and they have approximately equal variances) may not always be true for our data, the ANOVA results were verified with the more general Kruskal-Wallis H test (referred to as H test) which does not have any of these assumptions.

We quantify differences between new and previously published parameterizations with two metrics (results in Sect. 3.3): (i) the PD between W values obtained with different parameterizations; and (ii) significance tests (Student, ANOVA, and H) of the differences between W values obtained with new and previous W parameterizations.

2.4 Estimation of sea spray aerosol emissions

The newly formulated $W(U_{10}, T)$ parameterization is applied to estimate the global annual SSA emission using SSSF of M86 (Eq. (4)). Dividing Eq. (4) by Eq. (3), we modify the M86 SSSF to clearly separate the magnitude and shape factors (re-written here as Eq. (4′)):

$$\frac{dF}{dr_{80}} = W(U_{10}, T) \cdot \left[3.5755 \times 10^{5} \cdot r_{80}^{-3} (1 + 0.057 r_{80}^{1.05}) \times 10^{1.19 e^{-B^2}} \right] \qquad (4')$$

with B as defined in Sect. 1 and the timescale τ absorbed in the shape factor (the expression in the brackets). The size range for M86 validity is r_{80} = 0.8–8 μm. We calculate the SSA flux for radii r_{80} ranging from 1 to 10 μm.

2.4.1 Use of discrete whitecap method

The basic assumptions of M86 for the SSSF based on the discrete whitecap method—constant values for τ and dE/dr (Sect. 1)—are usually questioned (Lewis and Schwartz, 2004; de Leeuw et al., 2011; Savelyev et al., 2014). It is not expected for both of these assumptions to hold for wave breaking at various scales and under different conditions in different locations. The SSSF proposed by Smith et al. (1993) on the basis of measured size-dependent aerosol concentrations is one of the first formulations to demonstrate that the shape factor cannot be constant. Norris et al. (2013a) also demonstrated that the aerosol flux per unit area whitecap varies with the wind and wave conditions.

Recently, Callaghan (2013) showed that the whitecap timescale is another source of often overlooked variability in SSSF parameterizations based on M86. Because W typically includes foam from all stages of whitecap evolution, Callaghan (2013) suggested that the adequate timescale for the aerosol productivity from a discrete whitecap is not just its decay time (as in Eqs. (4) and (4′)), but the sum of the whitecap formation and decay timescales τ'. The value of τ' varies from breaking wave to breaking wave, but an area-weighted mean whitecap lifetime can be calculated for any given observational period to account for this natural variability. Analyzing the lifetimes of 552 oceanic whitecaps from a field experiment, Callaghan (2013) found that the area-weighted mean τ' varies by a factor of 2.7 (from 2.2 to 5.9 s). We refer the reader to Callaghan (2013) for an SSSF that accounts for SSA flux variability by explicitly incorporating whitecap timescale τ'.

Despite these questionable assumptions, the SSSF based on the discrete whitecap method in the form of M86 has been widely used in many models (Textor et al., 2006). Therefore, to those who have worked with M86 until now, a meaningful way to demonstrate how the new satellite-based W data, and W parameterizations based on them, would affect estimates of SSA flux is to hold everything else constant (e.g., the whitecap timescale and productivity in the shape factor) and clearly show differences caused solely by the use of new W expression(s) as a magnitude factor. On these grounds, the choice of the SSSF based on the M86 whitecap method is a suitable baseline for comparisons.

2.4.2 Choice of size distribution

Though the chosen size range of 1–10 μm for SSA particles is limited, it is well justified for the purposes of this study with the following arguments.

Generally, the division of the SSA particles into sizes of small, medium, and large modes (de Leeuw et al., 2011, their §8) is well warranted when one considers the climatic effect to be studied (Sect. 1). For example, sub-micron particles are important for scattering by SSA (direct effect) and the formation of cloud condensation nuclei (indirect effect), while super-micron particles are important for heat exchange (via sensible and latent heat fluxes) and heterogeneous chemical reactions (which need surface and volume to proceed effectively). However, in this study we do not focus on how the choice of the size distribution will affect the SSA estimates. Nor do we aim to present estimates of specific effect on the climate system. Rather, with a fixed size distribution, we explore how parameterizing W data, which carry information for the influences of many factors, would affect estimates of SSA emission (Sect. 1). In this sense, we can choose to use any published size distribution as a shape factor.

The chosen size range is the range of medium (super-micron) mode of SSA particles. This is the range for which the size distribution of M86 is valid (Sect. 2.4). The M86 size distribution, in its original or modified form, is widely used in GCMs and CTMs (Textor et al., 2006, their Table 3). This size range is a recurrent part of the various size ranges used in all (or at least most) SSSFs (see Table 2 in Grythe et al. (2014, hereafter G14)).

The chemical composition of the SSA particles is another argument favoring the chosen size range. The super-micron particles consist, to a good approximation, solely of sea salt, whereas, in biologically active regions, the sub-micron size range additionally includes

organic material, with an increasing contribution as particle size decreases (O'Dowd et al., 2004, Facchini et al., 2008; Partanen et al., 2014). Since the organic mass fraction in sub-micron SSA particles is still highly uncertain (Albert et al., 2012), we focus on the medium mode SSA emissions.

We evaluate the discrepancy expected due to neglecting particles below 1 μm using the G14 report of SSA production rate for dry particle diameters $D_p = r_{80}$ obtained with M86 over two different size ranges: 4.51×10^{12} kg yr^{-1} for the size range of 0.8 μm < r_{80} < 8 μm and 5.20×10^{12} kg yr^{-1} for size range of 0.1 μm < r_{80} < 10 μm. The different size ranges bring a difference between the two G14 estimates of about 14%. Neglecting particles with r_{80} < 0.1 μm would not change significantly the results presented here because they contribute on the order of 1% to the overall mass (Facchini et al., 2008).

Because total whitecap fraction, rather than only the active breaking crests, provides bubble-mediated production of SSA, we use W_{37} data to estimate the emission of medium mode SSA. The calculations use a modeling tool (Albert et al., 2010) in which the $W(U_{10})$ parameterization of MOM80, as integrated in Eq. (4), was replaced with the newly derived $W(U_{10}, T)$ parameterization (Eq. (4′)). The resulting size-segregated droplet number emission rate was converted to mass emission rate using the approximation $r_{80} = 2r_d \equiv D_p$, where r_d and D_p are the particle dry radius and diameter, respectively (e.g., Lewis and Schwartz, 2004; de Leeuw et al., 2011), and a density of dry sea salt of 2.165 kg m^{-3}.

3 Results and Discussion

The graphs showing our results visualize the W data points available for wind speeds from 0 to 35 m s^{-1}, but all fits are valid for $3 \le U_{10} \le 20$ m s^{-1} (Sect. 2.3).

3.1 Parameterization from global data set

Figure 5 shows global W data estimated from WindSat measurements for March 2006 as function of $U_{10QSCAT}$, at 10 GHz (Fig. 5a) and 37 GHz (Fig. 5b). For comparison, the MOM80 relationship (Eq. (3)) is also plotted in each panel. There are three noteworthy observations in Fig. 5. First, we note the different variability of W_{10} and W_{37} data. The 10 GHz data show far less variability than those at 37 GHz. The W_{37} data at a certain wind speed vary over a much wider range, with the strongest variability for wind speeds of 10-20 m s^{-1}. This supports the

suggestion that other variables, in addition to U_{10}, influence the whitecap fraction, such as SST or wave field; SAL13 quantify this variability.

Another observation in Fig. 5 is noted at low wind speeds. The 10 GHz scatter plot does not show W data for wind speeds lower than about 2 m s^{-1} because at these low wind speeds no active breaking occurs (Sect. 1). In contrast, non-zero W_{37} data are retrieved at wind speeds U_{10} < 2 m s^{-1}. Salisbury et al. (2013) suggested that the presence of foam on the ocean surface at these low wind speeds could be due to residual long-lived foam. This residual foam might be stabilized by surfactants, which increases its lifetime (Garrett, 1967; Callaghan et al., 2013). Another explanation could be production of bubbles and foam from biological activity (Medwin, 1977). However, there is not enough information currently to prove any of these conjectures.

The comparison of the MOM80 relationship (Eq. (3)) to W_{10} and W_{37} data clearly reveals the most important feature in Fig. 5—the wind speed dependence of satellite-based W data deviates from cubic and cubic-like relationship.

3.1.1 Wind speed dependence

Following the arguments of our approach (Sect. 2.1) and trying different expressions, we found that a quadratic wind speed exponent (n = 2) fits both W_{10} and W_{37} data sets best. For the same data shown in Fig. 5, Fig.6 shows the linear regression of the square root of W versus U_{10}:

$$\sqrt{W} = 0.01 U_{10} - 0.011 \qquad \text{10 GHz} \qquad (9a)$$

$$\sqrt{W} = 0.01 U_{10} + 0.019 \qquad \text{37 GHz} \qquad (9b)$$

with coefficients of correlation R^2 of 0.996 and 0.956, respectively. From Eq. (9), we obtain the following global average wind speed dependence of W using U_{10} from QuikSCAT:

$$W_{10} = 1 \times 10^{-4} (U_{10} - 1.1)^2 \qquad (10)$$

$$W_{37} = 1 \times 10^{-4} (U_{10} + 1.9)^2 \qquad (11)$$

where W is a fraction (not %).

The finding of weaker (quadratic) wind speed dependence here is not a precedent. The first reported $W(U_{10})$ relationship of Blanchard (1963) was quadratic. With careful statistical

considerations, Bondur and Sharkov (1982) derived a quadratic $W(U_{10})$ relationship for residual W (strip-like structures, in their terminology). Parameterizations of W in waters with different SST have also resulted in wind speed exponents around 2 (see Table 1 in Anguelova and Webster, 2006). Quadratic wind speed dependence is also consistent with the wind speed exponents of SAL13 in Eq. (1).

The y-intercept for W_{10} (Eq. (10)) is negative and, following the usual interpretation, yields a threshold wind speed of 1.1 m s^{-1} for whitecap inception. This is in the range of previously published values from 0.6 (Reising et al., 2002) to 6.33 (Stramska and Petelski, 2003). Meanwhile, the positive y-intercept b for W_{37} (Eq. (11)) is meaningless at first glance and intriguing upon some pondering. While foam from biological sources is possible (Sect. 3.1), it is not known whether such mechanism is capable of providing a measurable amount of foam patches which produce bubble-mediate sea spray efficiently.

We propose broader interpretation of b in Eqs. (10-11), be it negative or positive. Generally, it is expected that the atmospheric stability (Kara et al., 2008) and fetch (through the wave growth and development) cause inception of the whitecaps at lower or higher wind speed. One can consider the range of values for b mentioned above (0.6 to 6.33) as an expression of such influences. We suggest that b can also incorporate the effect of the seawater properties on the extent of W. The net result of all secondary factors may be either negative or positive b.

Specifically, we promote the hypothesis that a positive y-intercept b can be interpreted as a measure of the capacity of seawater with specific characteristics, such as viscosity and surface tension—which are governed by SST, salinity, and surfactant concentration—to affect W. Undoubtedly, none of these secondary factors creates whitecaps per se. Rather, they prolong or shorten the lifetime of the whitecaps via processes governed by the seawater properties. For instance, surfactants and salinity influence the persistence of submerged and surface bubbles. This yields variations of bubble rise velocity that replenishes the foam on the surface at different rates. Long-lived decaying foam added to foamy areas created by subsequent breaking events would augment W; conversely, conditions that shorten bubble lifetimes would reduce W (or at least not add to W).

A positive y-intercept can be thought of as a mathematical expression of this static forcing (as opposed to dynamic forcing from the wind) that given seawater properties can

sustain. That is, at any given location, this static forcing acts as though higher wind speed of magnitude (U_{10} + b) is producing more whitecaps than U_{10} alone. By parameterizing coefficients a and b in terms of different variables, one can evaluate how much the static forcing affects W in different geographic regions. By developing parameterizations $a(T)$ and $b(T)$ (Sect. 2.1), here we quantify only one static influence.

For completeness, we have also investigated the effect of either rising or waning winds on the $W(U_{10})$ relationship; increasing-decreasing winds are considered as a proxy for undeveloped-developed seas (Stramska and Petelski, 2003; CAL08). The rise-wane wind effect, as detected in this study, is not pronounced compared to findings in previous studies that use in situ wind speed data. Goddijn-Murphy et al. (2011) studied wind history and wave development dependencies on in situ W data using wave model (ECMWF), satellite (QuikSCAT), and in situ data for U_{10}. These authors detected significant effects only with in situ U_{10}. The absence of a significant wind history effect in our study might therefore be traced back to the method through which U_{10} was determined: wind speeds from satellites are spatial averages of scatterometric or radiometric observations that take a snapshot of the surface as it is affected by both history and local conditions, whereas in situ data for wind speed are single point values averaged over a short time and hence representative for a relatively small area. The effect of the spatial averaging of the satellite data over a much larger area (i.e., the satellite footprint) might be that information on wind history is lost in the process. The effect of the wind history, therefore, is not further sought in this study.

3.1.2 Intrinsic correlation

To quantify the possible intrinsic correlation in the derived $W(U_{10})$ parameterization (Eqs. (10-11)), we derived $W(U_{10})$ using ECMWF wind speeds instead of the QuikSCAT wind speeds (Sect. 2.3). Figure 7 shows a scatter plot of $W^{1/2}$ versus $U_{10\mathrm{ECMWF}}$ (only data for 37 GHz are shown); dashed and solid lines show unconstrained and zero-forced fits, respectively. The linear regression (given in the figure legend) is used to obtain the global average wind speed dependence using U_{10} from ECMWF as follows:

$$W_{37} = 8.1\times10^{-5}\left(U_{10}+3.33\right)^2 \qquad (12).$$

The positive intercept here is interpreted as in Sect. 3.1.1.

To evaluate the significance of the intrinsic correlation, we look at the change of the correlation coefficient of the $W(U_{10})$ relationship when QuikSCAT winds are substituted with the ECMWF winds. Physically, we expect a strong correlation between $w^{1/2}$ and U_{10}, and we see this clearly in Fig. 6b which shows a correlation coefficient R^2 = 0.956 for $w^{1/2}$ and $U_{10QSCAT}$. However, the correlation coefficient might not be as high as in Fig. 6 if U_{10} were from a more independent source. We see this when comparing Figs. 6b and 7. The $w^{1/2}$–U_{10} correlation is still strong in Fig. 7, but the plot shows more scatter and slightly lower correlation with R^2 = 0.826. This is a sign that probably some intrinsic correlation contributes to the $W(U_{10QSCAT})$ relationship which, therefore, is stronger than $W(U_{10ECMWF})$.

The slopes in Figs. 6b and 7 differ by about 11%. We evaluate how this translates into differences in W_{37} values using Eqs. (11) and (12). We found the PD between W_{37} ($U_{10QSCAT}$) and $W_{37}(U_{10ECMWF})$ to be less than ± 9% for wind speeds of 7–23 m s^{-1}. Specifically, the W_{37} values obtained with $U_{10QSCAT}$ and $U_{10ECMWF}$ are equal for wind speed of 11 m s^{-1}. Below 11 m s^{-1}, $W_{37}(U_{10ECMWF})$ is higher than $W_{37}(U_{10QSCAT})$ by up to 8.8%. Above 11 m s^{-1}, $W_{37}(U_{10ECMWF})$ is smaller than $W_{37}(U_{10QSCAT})$ by up to 8.4%. The difference goes up to 30% for wind speeds of 3 m s^{-1}.

While R^2 values for the regressions in Figs. 6b and 7 suggest that the intrinsic correlation may contribute to these differences, this is not the only possible reason for the discrepancies. The difference of about 5% between the U_{10} values from the two different sources (Fig. 4a) also contributes to the W discrepancies from Eqs. (11) and (12). Of course, we have to consider these differences in the light of other uncertainties in Eqs. (11) and (12) such as the uncertainties in determining $U_{10QSCAT}$ and $U_{10ECMWF}$ and the satellite-based W data itself. We, therefore, conclude that the effect of the intrinsic correlation alone on W is most likely less than about 4% for most wind speeds.

3.2 Regional and seasonal analyses

3.2.1 Magnitude of regional and seasonal variations

Figure 8 shows examples of the $w^{1/2}$ versus $U_{10QSCAT}$ for different regions and seasons. Figures 8a and 8b show scatter plots for the Gulf of Mexico (region 1) at both frequencies for January 2006. Statistics are presented at the top of the figures and the fit lines are shown in red. Figures 8c and 8d show the fit lines $w^{1/2}(U_{10})$ for 10 and 37 GHz in region 5

for all months, while Figs. 8e and 8f demonstrate variations of the fit lines $W^{1/2}(U_{10})$ for both frequencies over all regions for March 2006. Figure 8 shows that the variations of the $W^{1/2}(U_{10})$ relationships at 10 GHz are smaller than those for 37 GHz, confirming the same observation reported by SAL13 but obtained with a different analysis. Focusing on the results for 37 GHz, we note that geographic differences from region to region for a fixed time period (Fig. 8f) yield more variability in the $W^{1/2}(U_{10})$ relationship than seasonal variations at a fixed location (Fig. 8d).

Figure 9 shows the seasonal cycles of m and c of the $W^{1/2}(U_{10})$ relationships at 37 GHz in regions 4, 5, 6, and 12. The annual variations of each curve and the variations between the curves confirm the observation from Fig. 8—the variations of m and c over the year are smaller than their variations from region to region. Figure 9 also shows that the seasonal cycles of m and c do not mimic the seasonal cycles of either U_{10} or T (Fig. 3). This implies that m and c are not merely scaling and offsetting the $W^{1/2}(U_{10})$ relationships, as Eq. (8) suggests, but rather carry more information for the regional and seasonal influences.

As anticipated from Figs. 8a, 8c, and 8e, seasonal cycles for the 10 GHz data reveal much less regional and seasonal influences (not shown). Because the 37 GHz data provide more information for secondary forcing than the 10 GHz data, the remainder of the data analysis in this study is illustrated with results for W_{37} data. Note, however, that all the procedures and analyses described for W_{37} data have been also carried out for the W_{10} data and some final results are reported (e.g., sect. 3.3.2).

Figures 8 and 9 show that variations of $W^{1/2}$ caused by U_{10} from 3 to 20 m s^{-1} are much larger than the regional and seasonal variations of $W^{1/2}$. While this is expected (because U_{10} is a primary forcing factor), this also points that we need to evaluate whether these regional and seasonal variations are statistically significant. For this, we grouped the data for m and c, as well as for a and b, in two ways: (1) by month with the full range of geographical variability (over all 12 regions) for each month; and (2) by region with the full range of seasonal variability (over all 12 months) for each region. ANOVA and H tests applied to both groups showed that the seasonal variations are not statistically significant, while the regional variations are.

We illustrate this in Fig. 10 with values for b; similar graphs for m, c, and a show the same results. Figure 10a shows the seasonal cycle for the regionally averaged b values with

error bars (± one SD) representing the regional variability. It is clear that the seasonal variations of the regionally averaged *b* values lay within the regional variability. This suggests that variations of *b* from month to month are statistically undistinguishable. Figure 10b illustrates why variations of *b* from region to region are significantly different. The graph shows the annually averaged *b* values for each region with error bars representing the seasonal variability. It is clear that overall the geographical variations are not lost in the seasonal variability.

Note in Fig. 10b that some regional variations might not be distinguished within their seasonal variability. For example, the annual means for regions 1, 4, 7, 8, and 9 all lay within their seasonal variability; likewise, for the annual means for regions 5, 9, and 10. To pinpoint regions with significant differences of *b* (as well as *a*, *m*, and *c*), we applied the Student test to all possible pairs of regions; e.g., region 1 paired with each region from 2 to 12, region 2 paired with each region from 3 to 12, and so on to a total of 66 pairings of different regions. The Student tests showed statistically different values of *b* from region to region in 78% of all cases and 58% for *a*.

3.2.2 Quantifying SST variations

The results of the significance tests give a rationale for developing the SST dependences $a(T)$ and $b(T)$. Following the data representation in Fig. 10b, we derived $a(T)$ and $b(T)$ for data at 37 GHz by relating annually averaged *a* and *b* values to the annually averaged *T* for each region (Fig. 11). Figure 11c shows the monthly means of the coefficients *b* for each region and thus demonstrates how the data points in Fig. 11b have been formed; a similar procedure is used for the data points in Fig. 11a. As in Fig. 10b, the error bars (± one SD) represent the seasonal variability for SST (horizontal bars) and the coefficients *a* and *b* (vertical bars). A second order polynomial is fitted to the data points in Fig. 11a; a linear fit is applied to the data in Fig. 11b. The correlation coefficients for the derived SST dependences are $R^2 = 0.57$ for $a(T)$ and $R^2 = 0.87$ for $b(T)$. Such R^2 values are consistent with the expectation that SST, being a static secondary factor, affects *W* more via the offset *b* than via the slope *a*.

To evaluate the effect of using quadratic versus cubic wind speed dependence in Eq. (8), we also derived the SST dependences $a(T)$ and $b(T)$ for $n = 3$ following the same procedure as for the case of $n = 2$. We applied Eq. (8) with $n = 3$ (Eq. (5b)) to W_{37} data for all months in regions 4, 5, 6, and 12; we verified that differences due to the use of four instead of

twelve regions are not significant. The absolute values of m and c increase compared to their values obtained with $n = 2$. Specifically, the slopes m in each of the four regions change by 30% to 50%, while their regional variability (i.e., SD) increased by a factor of 3. The y-intercepts c in the four regions become larger than the c values obtained with $n = 2$ by a factor of 4.6, with regional variability increasing by a factor of 2. However, put together, the fit lines $W^{1/3}(U_{10})$ in region 5 for all months and in all four regions for March 2006 (not shown) behave like those in Figs. 8d and 8f; namely, seasonal variations are smaller than variations from region to region. Coefficients a and b are calculated from the m and c values and graphs similar to those in Fig. 11 are produced. Linear fits for both a and b were applied to these graphs. The correlation coefficients for these fits are $R^2 = 0.87$ for $a(T)$ and $R^2 = 0.91$ for $b(T)$.

The reason for the different values of m and c (thus a and b) for different n is that each set of coefficients (n, m, c) accounts for primary (i.e., U_{10}) and secondary factors differently. When the expected cubic law is applied to regional data sets which exhibit quadratic wind speed dependences (following from Figs. 5-6), the large differences are reconciled solely by m and c; their values are therefore high. Conversely, smaller values for m and c are required to quantify regional variations when the wind speed exponent is already adjusted to follow the quadratic trend of the data. This confirms the reasoning in Sect. 2.1 that the change from cubic to quadratic wind speed exponent is a major change that the additional parameters impart on the $W(U_{10})$ relationship. The question then is which set of parameters—($n = 2$, m, c) or ($n = 3$, m, c)—better reproduce measured W data. In other words, if the wind speed exponent n is not adjusted but follows the physically determined cubic dependence, can the parametric coefficients m and c alone account for all observed variations of W? We quantify and discuss this point in Sect. 3.3.

3.3 New parameterization of whitecap fraction

A new parameterization for the whitecap fraction $W(U_{10}, T)$ was obtained by replacing the fixed coefficients $A = 1\times10^{-4}$ and $B = 1.9$ in Eq. (11) with SST-dependent coefficients:

$$W = a(T)\left[U_{10} + b(T)\right]^2 \tag{13}$$

where

$$a(T) = a_0 + a_1 T + a_2 T^2 \tag{14a}$$

$$b(T) = b_0 + b_1 T \tag{14b}$$

and the coefficients are:

$a_0 = 8.462\times10^{-5}$

$a_1 = 1.625\times10^{-6}$

$a_2 = -3.348\times10^{-8}$ (14c)

$b_0 = 3.354$

$b_1 = -6.206\times10^{-2}$

The whitecap fraction is calculated with Eqs. (10-12 and 13-14) and compared to both parameterized W values and to W data. The W values from SAL13 (37 GHz) and MOM80 are used as references for PD calculations and significance tests (Sect. 2.3).

3.3.1 Comparisons to *W* parameterizations

All parameterizations shown here are run for wind speeds from 3 to 20 m s^{-1}. The global quadratic $W(U_{10})$ (Eq. (11)) is compared to the published parameterizations of SAL13 (at 10 and 37 GHz), CAL08, and MOM80 (Eqs. (1-3)) in Fig. 12a. The PD between the global quadratic $W(U_{10})$ and SAL13 at 37 GHz ranges from 0.5% to 10% over the wind speed range. ANOVA and Student tests show that such differences are not statistically significant. That is, the global quadratic $W(U_{10})$ parameterization replicates the trend of the satellite-based W data as well as the SAL13 parameterization, which has a more specific wind speed exponent. Note that we do not expect our $W(U_{10})$ parameterization to be distinctly different from that of SAL13 because both studies use the same W database.

The PD between the trends of the global quadratic $W(U_{10})$ and MOM80 $W(U_{10})$ is from 5% up to 175% with the largest PDs for wind speeds below 7 m s^{-1}. Though Fig. 12a shows visibly different trends from both parameterizations, they seem to fall within each other uncertainties because both ANOVA and Student tests show no significant difference between them. However, if applied for winds up to 25 m s^{-1} (Table 1), significant differences occur. That is, the use of the new global quadratic $W(U_{10})$ expression brings important changes to the trend of W compared to that from MOM80 $W(U_{10})$ at high winds.

Figure 12b shows W values from the new $W(U_{10}, T)$ parameterization at three fixed SST values (T = 28, 12, and 1 °C); the parameterizations of SAL13 for 37 GHz and MOM80 are shown for reference. Physically (from the SST dependence of the seawater viscosity), at

the same wind speed, W is expected to be higher in warm waters and lower in cold waters (Monahan and Ó'Muircheartaigh, 1986). Figure 12b shows a more complicated behavior of W. The highest W values (green line) are for moderate SST of 12 to 20 °C. At extreme SSTs (2 and 28 °C, blue and red lines, respectively), the SST influence on W changes depending on the wind speed: W is the lowest in cold waters and high winds, but is higher than W in warm waters at low winds. The trends of coefficients a and b in Fig. 11 suggests that we can expect such reversal.

According to Fig. 12b, changes of SST from 1 to 28 °C bring relatively small variations in the wind speed trend of W, PD no more than 15%. Applying Student tests, we find that the W values at any T remain statistically the same. In addition, W values at any T are not significantly different from the W predictions of the global quadratic $W(U_{10})$ parameterization. These results support the anticipated notion (Sect. 3.2.2) that by using quadratic wind speed exponent either in $W(U_{10})$ or $W(U_{10}, T)$, we can indeed account implicitly (i.e., only via adjustment of the U_{10} exponent) for most of the SST (and other) influences.

Figure 12c compares W values obtained with the quadratic and cubic $W(U_{10}, T)$ parameterizations at T = 20 °C; MOM80 and SAL13 at 37 GHz are shown for reference. With $p > 0.05$ for any fixed T, the W values from the cubic $W(U_{10}, T)$ parameterization are not statistically different from those obtained with either the quadratic $W(U_{10}, T)$ or MOM80. Still, the different trends of the W values seen in Fig. 12c suggest that accounting explicitly for SST via $a(T)$ and $b(T)$ in the physically expected cubic wind speed dependence is not sufficient to replicate the satellite-based W values. That is, when using n = 3, one needs to include more secondary forcing in order to reproduce the weaker wind speed dependence from the W database.

3.3.2 Comparisons to *W* data

Comparisons to the published in situ W data demonstrate order-of-magnitude consistency of the W values from the new parameterizations. Because there are no other remotely-sensed W data except those from WindSat, the most we can do at the moment is to evaluate how well the new parameterizations can replicate the trend and the spread of the satellite-based W. Recently, W values from a global wave model were compared to W from MOM80 and WindSat by Leckler et al. (2013), so one can evaluate where modeled W values stand in the

comparison of data and parameterizations of W. All parameterized W values shown here are calculated using U_{10} and T from the whitecap database, i.e., U_{10} from QuikSCAT and T from GDAS (Sect. 2.2.1).

Figure 13a compares W values predicted with both new parameterizations, $W(U_{10})$ and $W(U_{10}, T)$, to the same in situ and satellite-based W data for 10 and 37 GHz plotted in Fig. 1b; comparisons to satellite-based W data on any other day of 2006 are the same. Once again, it is confirmed that the new global quadratic $W(U_{10})$ parameterizations (black symbols in the figure) follow closely the wind speed trends of the satellite-based W data. This lends confidence in the use of the proposed quadratic $W(U_{10})$ parameterization to model the W trend with secondary influences implicitly included.

The W values predicted with the new $W(U_{10}, T)$ parameterization (red and cyan symbols in Fig. 13a) represent the spread of the satellite-based W data fairly well; tests show that they do not differ significantly. The cluster of W values are, however, statistically different from both the new quadratic and the MOM80 $W(U_{10})$ parameterizations. This is the most important result of this study: when we model only the trend of W with U_{10}, new and old parameterizations differ significantly only for extreme conditions (e.g., winds above 20 m s^{-1} in cold waters, Sect. 3.3.1). In contrast, when we model both the trend *and* the spread of the W values, the result is a significant difference with any, new or old, $W(U_{10})$ parameterization at any conditions.

In Fig. 13a, one can notice that the new $W(U_{10}, T)$ parameterization does not predict the spread of the satellite-based W data entirely. This suggests that accounting explicitly for SST in a W parameterization is not enough to replicate all the natural variability of W. This is consistent with our general understanding of the need to explicitly include many secondary factors in W parameterizations, not just SST (Sect. 2.1).

Though SST entails small variations in the trend of W with U_{10} (Fig. 12b), the most important consequence of the newly derived quadratic $W(U_{10}, T)$ parameterization is that it shapes significantly different spatial distribution compared to cubic and higher wind speed dependences like that of the MOM80. The complex behavior seen in Fig. 12b attests to this because different combinations of SST and U_{10} could be encountered over the globe. Meanwhile, the recreation of the spread of the satellite-based W data in Fig. 13a confirms that a $W(U_{10}, T)$ expression can model such situations.

Figure 13b shows a difference map between the global annual average W distributions for 2006. The MOM80 relationship yields a wider W range with higher values in regions with the highest wind speeds. In particular, this occurs between about 40° and 70° in the Southern ocean and in the North Atlantic. The latitudinal variations from the Equator to the poles are more pronounced when using the MOM80 relationship as compared to Eqs. (13-14). The new $W(U_{10}, T)$ parameterization provides a global spatial distribution with similar patterns, but the absolute values are lower at high latitudes and higher at low latitudes.

Note that in most studies, as in this study, $W(U_{10})$ of MOM80 is extrapolated beyond the range of the data from which it was derived (Sect. 1). Therefore, at higher wind speeds (and especially in cold waters), the W values that are obtained using the MOM80 parameterization are somewhat questionable. At the same time, the QuikSCAT instrument, which provided the U_{10} satellite data used in this study, has a decreased sensitivity for wind speeds over 20 m s^{-1} (Quilfen et al., 2007). All results regarding higher wind speeds should, therefore, be handled with caution. Only continuous comparison of directly measured W data to parameterized W values can help to better constrain predictions of whitecap fraction.

3.4 Sea spray aerosol production

The newly derived quadratic $W(U_{10}, T)$ parameterization (Eqs. (13-14)) was used to estimate the global annual average emission of super-micron SSA using M86 SSSF (Eq. (4′)). The total (i.e., size integrated) annual SSA mass emission for 2006 is 4359.69 Tg yr^{-1} (4.4×10^{12} kg yr^{-1}). This is about 50% larger than that calculated with the M86 SSSF using MOM80 (Eq. (4)), 2915 Tg yr^{-1} (2.9×10^{12} kg yr^{-1}). Because we have shown that the new quadratic $W(U_{10}, T)$ and MOM80 $W(U_{10})$ are significantly different (Sect. 3.3.2), we infer that the SSA emissions based on SSSFs using these two parameterizations also differ significantly. The two estimates of SSA emissions are calculated using the same modelling tool (Sect. 2.4) and the same input data (Sect. 2.2.1). Without any change in the shape factor, this guarantees that the 50% difference is due solely to the explicit accounting for the SST effect on W.

The spatial distribution of the mass emission rates obtained with SSSFs using the new $W(U_{10}, T)$ is shown in Fig. 14a. The SSA emissions obtained with the new and the MOM80 $W(U_{10})$ parameterizations mimic the patterns of the W distributions. The differences are mapped in Fig. 14b.

Previously modeled total dry SSA mass emissions vary by two orders of magnitude because of a variety of uncertainty sources (Sect. 1): $(2.2–22)\times10^{12}$ kg yr^{-1} (Textor et al., 2006, their Fig. 1a; de Leeuw et al., 2011, their Table 1); and $(2–74)\times10^{12}$ kg yr^{-1} for long-term averages (over 25 years) (G14, their Table 2, excluding 3 outliers). The impact of the modeling method used has to be acknowledged too. Grythe et al. (2014) suggest that the spread in published estimates of global emission based on the same M86 SSSF (Eq. (4)), from 3.3×10^{12} to 11.7×10^{12} kg yr^{-1} (Lewis and Schwartz, 2004), can be attributed to differences in model input data and resolution differences. An example of the same SSSF yielding different results when applied in different models is also seen in the work of de Leeuw et al. (2011, their Table 1).

For a meaningful comparison of our results to SSA emissions obtained with other SSSFs, we attempt to remove (or at least minimize) the impact of the modeling method. As in this study, G14 used the same model (i.e., input data and configuration) to evaluate 21 SSSFs, including that of M86, against measurements. We thus can infer a "modelling" factor using our and G14 results obtained with M86 SSSF. We find that the G14 estimate of SSA emission from M86 (4.51×10^{12} kg yr^{-1}) is 1.55 times larger than our estimate of 2.9×10^{12} kg yr^{-1} from M86 and MOM80. We apply this factor of 1.55 to our SSA emission estimated with the new $W(U_{10}, T)$ parameterization and obtain a "model scaled" value of 6.75×10^{12} kg yr^{-1}. Our "model scaled" estimate of the SSA emission is close to the median 5.91×10^{12} kg yr^{-1} of the SSA emissions reported by G14. This shows that an SSSF with a magnitude factor derived from satellite-based W data provides reasonable and realistic predictions of the SSA emission.

To narrow down this broad assessment, we now look at the SSSFs evaluated by G14 which account for the SST effect on SSA emissions. There are four such SSSFs in the G14 study (see their Table 2): S11T of Sofiev et al. (2011), G03T of Gong (2003), J11T of Jaeglé et al. (2011), and G13T of G14. To minimize differences caused by using different size ranges, we focus on S11T and G13T, both applied to dry SSA diameters $D_p = r_{80}$ (Sect. 2.4) from 0.01 to 10 μm. The upper limit is the same as in our study, while the lower limit is extended to sub-micron sizes, which, as we have seen (Sect. 2.4.2), introduces a discrepancy of about 14%.

The original Sofiev et al. (2011) SSSF is based on the M86 SSSF (Eq. (4)) combined with data from laboratory experiments by Mårtensson et al. (2003) to account for SST and

salinity effects and a field experiment by Clarke et al. (2006) to extend the size range. In the G14 study, the salinity weight proposed by Sofiev et al. (2011) is not applied. At a reference salinity of 33 ‰, S11T estimates an SSA emission of 2.59×10^{12} kg yr^{-1}. Without the SST effect (the SST factor set to unity), the SSA emission estimated with S11 is 5.87×10^{12} kg yr^{-1}. With everything else the same except for the SST factor in source functions S11 and S11T, we evaluate that accounting for the SST effect results in changes by 56%. Correcting for 14% discrepancy due to extended lower size limit, we infer a 42% change when the SST effect is included in the SSSF. This is comparable to the 50% change due to SST in our case. We surmise that parameterizing additional influences on W is a viable way to account and explain some of the uncertainty of SSA emissions.

Grythe et al. (2014) used a large data set of ship observations to develop G13T by changing both the magnitude and the shape factors. The authors modified the SSSF of Smith and Harrison (1998) (a sum of two log-normal distributions) to add an extra log-normal mode to cover the accumulation mode. They also added the empirically based SST factor (a third order polynomial) proposed by Jaeglé et al. (2011). With G13T, G14 estimate an SSA emission of 8.91×10^{12} kg yr^{-1}. The functional forms of the magnitude (involving the SST effect) and shape (modelling the size distribution) factors of G13T and S11T are very different. This makes it difficult to evaluate the relative contribution of the magnitude and shape factors for variations in SSA emissions. Our results can help.

The shape factors of S11T and our SSSF using $W(U_{10}, T)$ have a similar (not identical) functional form (that of M86, original and modified), but the functional forms accounting for SST are different. Our SSA emission estimate is about 62% higher than that of S11T. Allowing for 14% discrepancy due to the lower size limit, we find that different approaches to account for SST lead to about 67% variation in SSA emissions. Compared to G13T, our SSSF using $W(U_{10}, T)$ has a different shape factor (that of M86 versus log-normal), and a similar (but not identical) functional form for the SST effect (polynomial). Our SSA emission estimate is about 32% lower than that of G13T. Allowing for 14% size discrepancy, we find that different shape factors lead to about 13% variation in SSA emissions.

On the basis of these assessments, we can state that the inclusion of the SST effect in the magnitude factor and/or the choice of the shape factor (size range and model for the size distribution) in the SSSF can explain 13%-67% of the variations in the predictions of SSA emissions. The spread in SSA emission can thus be constrained by more than 100% when

improvements of both the magnitude and the shape factor are pursued. Our results on the W parameterization (Fig. 13a) suggest that accounting for more secondary forcing in the magnitude factor would explain more fully the spread among SSA emissions. Because, after wind speed, the most important secondary factor that accounts for variability in W is the wave field (SAL13), efforts to include wave parameters in W parameterizations are well justified.

4 Conclusions

The objective of the study presented here is to evaluate how accounting for natural variability of whitecaps in the parameterization of the whitecap fraction W would affect mass flux predictions when using a sea spray source function based on the discrete whitecap method. The study uses satellite-based W data estimated from measurements of the ocean surface brightness temperature T_B by satellite-borne microwave radiometers at frequencies of 10 and 37 GHz, W_{10} and W_{37}. Global and regional data sets comprising W_{10} and W_{37} data, wind speed U_{10}, and sea surface temperature T for 2006 were used to derive parameterizations $W(U_{10})$ and $W(U_{10}, T)$. The SSSF of Monahan et al. (1986) combined with the new $W(U_{10}, T)$ was used to estimate sea spray aerosol emission. The conclusions of the study are the following.

Assessment of the global W data set revealed a quadratic correlation between W and U_{10} (Eqs. (10-11)). The unconventional positive y-intercept for $W_{37}(U_{10})$ could be interpreted as a mathematical expression of the static forcing that given seawater properties (e.g., effects of SST, salinity, and surfactant concentrations) impart on whitecaps. Parameterization $W(U_{10})$ derived with an independent data set (U_{10} from ECMWF instead of QuikSCAT) helps to determine that the intrinsic correlation between W and U_{10} is most likely less than about 4%. The derived $W(U_{10})$ for both W_{10} and W_{37} replicate the trend of the satellite-based data well (Fig. 13a). That is, the adjusted quadratic wind speed exponent in $W(U_{10})$ accounts implicitly for most of the SST variations. The new quadratic $W(U_{10})$ predicts whitecap fraction significantly different from that obtained with the widely used $W(U_{10})$ of MOM80 only at extreme conditions (high winds and cold waters).

Applying the global quadratic $W(U_{10})$ parameterization on regional scale shows that the seasonal variations of its regression coefficients a and b are not statistically significant, while the regional variations are. On this basis, by relating annually averaged a and b values to the annually averaged T for each region (Fig. 11), the SST dependences $a(T)$ and $b(T)$ for data at 37 GHz were derived. The new quadratic $W(U_{10}, T)$ parameterization (Eqs. (13-14))

predicts small variations in the trend of W for different SST values (Fig. 12b). However, when used with real U_{10} and T data, the new $W(U_{10}, T)$ parameterization replicates the variability (spread) of the satellite-based W data well (Fig. 13a). The capability of the new $W(U_{10}, T)$ parameterization to model both the trend and the spread of the W data sets it apart from all other $W(U_{10})$ parameterizations. Results show that besides SST, one needs to include explicitly other secondary factors in order to model the full spread of the satellite-based W. Including the SST effect via $a(T)$ and $b(T)$ in the physically expected cubic wind speed dependence is not sufficient to replicate the trend of the satellite-based W values.

Application of the new quadratic $W(U_{10}, T)$ parameterization in the Monahan et al. (1986) SSSF resulted in a total (integrated only over super-micron sizes) SSA mass emission estimate of 4359.69 Tg yr^{-1} (4.4×10^{12} kg yr^{-1}) for 2006. Scaled for modeling differences (Sect. 3.4), this estimate is 6.75×10^{12} kg yr^{-1}, which is comparable to previously reported estimates. Comparing our and previous total SSA emissions, we have been able to assess to what degree accounting for the SST influence on whitecaps can explain the spread of SSA emissions. With or without the SST effect included in the SSSF, SSA emissions obtained with the new $W(U_{10}, T)$ parameterization vary by ~50%. Different approaches to account for SST effect yield ~67% variations. Different models for the size distribution applied to different size ranges lead to 13%-42% variations in SSA emissions. Understanding and constraining the various sources of uncertainty in the SSSF would eventually improve the accuracy of SSSF predictions. Including the natural variability of whitecaps in the SSSF magnitude factor is a viable way toward such accuracy improvement.

Data availability

The data analysis and the results reported in this study are available from the corresponding author M.F.M.A. (Monique) Albert (mfmaalbert@gmail.com).

Acknowledgements

This study is partly funded by SRON, Netherlands Institute for Space Research, through the Dutch Users Support Programme GO-2. MDA was sponsored by the Office of Naval Research, NRL Program element 61153N, WU 4500. GdL by was supported by the European Space Agency (Support to Science Element: Oceanflux Sea Spray Aerosol, contract No. 4000104514/11/I-AM), the Centre on Excellence in Atmospheric Science funded by the

Finnish Academy of Sciences Excellence (project no. 272041), the CRAICC project (part of the Top-level Research Initiative).

References

Albert, M. F. M. A., Schaap, M., de Leeuw, G., and Builtjes, P. J. H.: Progress in the determination of the sea spray source function using satellite data, Journal of Integrative Environmental Sciences, 7, 159-166, 2010.

Albert, M. F. M. A., Schaap, M., Manders, A. M. M., Scannell, C., O'Dowd, C. D., and de Leeuw, G.: Uncertainties in the determination of global sub-micron marine organic matter emissions, Atmos. Environ., 57, 289-300, 2012.

Andreae, M. O. and Crutzen, P. J.: Atmospheric aerosols: biogeochemical sources and role in atmospheric chemistry, Science, 276, 1052-1058, 1997.

Andreas, E. L.: Sea Spray and the turbulent air-sea heat fluxes, J. Geophys. Res., 97, 11429-11441, 1992.

Anguelova, M. D. and Gaiser, P. W.: Skin depth at microwave frequencies of sea foam layers with vertical profile of void fraction, J. Geophys. Res., 116, C11002, 2011.

Anguelova, M. D. and Gaiser, P. W.: Microwave emissivity of sea foam layers with vertically inhomogeneous dielectric properties, Remote Sens. Environ., 139, 81-96, 2013.

Anguelova, M. D. and Webster, F.: Whitecap coverage from satellite measurements: A first step toward modeling the variability of oceanic whitecaps. J. Geophys. Res., 111, C03017, 2006.

Anguelova, M. D., Bettenhausen, M. H., and Gaiser, P. W.: Passive remote sensing of sea foam using physically-based models, in: Proceedings of the IGARSS 2006: IEEE International Geoscience and Remote Sensing Symposium, Denver, Colorado, USA, 31 July-4 August, 3659-3662, 2006.

Anguelova, M. D., Bettenhausen, M. H., Johnston, W. F., Gaiser, P. W.: First extensive whitecap database and its use to study whitecap fraction variability, in: Proceedings of the 17th Air-Sea Interaction Conference, AMS, Annapolis, Maryland, USA, 26 - 30 September, 2010 (http://ams.confex.com/ams/pdfpapers/174036.pdf).

Anguelova, M. D., Bobak, J. P., Asher, W. E., Dowgiallo, D. J., Moat, B. I., Pascal, R. W., and Yelland, M. J.: Validation of satellite-based estimates of whitecap coverage: approaches and initial results, in: Proceedings of the 16th Air-Sea Interaction conference, AMS, Phoenix, Arizona, USA, 10-15 January, 2009, (http://ams.confex.com/ams/pdfpapers/143665.pdf).

Asher, W. E. and Wanninkhof, R.: The effect of bubble-mediated gas transfer on purposeful dual-gaseous tracer experiments, J. Geophys. Res., 103, 10,555-10,560, 1998.

Barrie, L. A., Bottenheim, J. W., Schnell, R. C., Crutzen, P. J., and Rasmussen, R. A.: Ozone destruction and photochemical reactions at polar sunrise in the lower Arctic atmosphere, Nature, 334, 138–141, 1988.

Bettenhausen, M. H., Smith, C. K., Bevilacqua, R. M., Wang, N. –Y., Gaiser, P. W., and Cox, S.: A nonlinear optimization algorithm for WindSat wind vector retrievals, IEEE T. Geosci. Remote, 44, 597-610, 2006.

Blanchard, D. C.: The electrification of the atmosphere by particles from bubbles in the sea, Prog. Oceanogr., 1, 73-112, 1963.

Blanchard, D. C.: The production, distribution, and bacterial enrichment of the sea-salt aerosol, in: Air-sea exchange of gases and particles, Liss, P. S. and Slinn, W. G. N., D. Reidel Publishing Company, Dordrecht, The Netherlands, 407-454, 1983.

Bondur, V., and Sharkov, E.: Statistical properties of whitecaps on a rough sea, Oceanology, 22, 274– 279, 1982.

Callaghan, A. H.: An improved whitecap timescale for sea spray aerosol production flux modeling using the discrete whitecap method, J. Geophys. Res.-Atmos., 118, 9997-10010, 2013.

Callaghan, A. H. and White, M.: Automated processing of sea surface images for the determination of whitecap coverage, J. Atmos. Ocean. Tech., 26, 383-394, 2009.

Callaghan, A. H., de Leeuw, G., Cohen, L., and O'Dowd, C. D.: Relationship of oceanic whitecap coverage to wind speed and wind history, Geophys. Res. Lett., 35, L23609, 2008.

Callaghan, A. H., Deane, G. B., and Stokes, M. D.: Two Regimes of Laboratory Whitecap Foam Decay: Bubble-Plume Controlled and Surfactant Stabilized, J. Phys. Oceanogr., 43, 1114-1126, 2013.

Chameides, W. L. and Stelson, A. W.: Aqueous-phase chemical processes in deliquescent sea-salt aerosols: a mechanism that couples the atmospheric cycles of S and sea salt, J. Geophys. Res.- Atmos., 97, 20565-20580, 1992.

Chelton, D. B. and Freilich, M. H.: Scatterometer-based assessment of 10-m wind analyses from the operational ECMWF and NCEP numerical weather prediction models, Mon. Weather Rev., 133, 409-429, 2005.

Cicerone, R. J.: Halogens in the atmosphere, Rev. Geophys. Space Ge., 19 (NO. 1), 123-139, 1981.

Clarke, A. D., Owens, S. R., and Zhou, J.: An ultrafine sea-salt flux from breaking waves: Implications for cloud condensation nuclei in the remote marine atmosphere, J. Geophys. Res., 111, D06202, 2006.

de Leeuw, G., Andreas, E. L., Anguelova, M. D., Fairall, C. W., Lewis, E. R., O'Dowd, C. D., Schulz, M., and Schwartz, S. E.: Production flux of sea-spray aerosol, Rev. Geophys., 49, RG2001, 2011.

Facchini, M. C., Rinaldi, M., Decesari, S., Carbone, C., Finessi, E., Mircea, M., Fuzzi, S., Ceburnis, D., Flanagan, R., Nilsson, E. D., de Leeuw, G., Martino, M., Woeltjen, J., and O'Dowd, C. D.: Primary submicron marine aerosol dominated by insoluble organic colloids and aggregates, Geophys. Res. Lett., 35, L17814, 2008.

Fairall, C. W., Kepert, J. D., and Holland, G. J.: The effect of sea spray on surface energy transports over the ocean, The Global Atmosphere and Ocean System, 2, 121-142, 1994.

Falkowski, P. G., Barber, R. T., and Smetacek, V.: Biogeochemical controls and feedbacks on ocean primary production, Science, 281, 200-206, 1998.

Ghan, S. J., Guzman, G., and Hayder, A. -R.: Competition between sea salt and Sulfate particles as cloud condensation nuclei, J. Atmos. Sci., 55, 3340-3347, 1998.

Gaiser, P.W., St. Germain, K. M., Twarog, E. M., Poe, G. A., Purdy, W., Richardson, D., Grossman, W., Linwood Jones, W., Spencer D., Golba, G., Cleveland, J., Choy, L., Bevilacqua, R. M., and Chang, P. S.: The WindSat spaceborne polarimetric microwave radiometer: sensor description and early orbit performance, IEEE T. Geosci. Remote, 42, NO. 11, 2347–2361, 2004.

Garrett, W. D.: Stabilization of air bubbles at the air-sea interface by surface-active material, Deep-Sea Res., 14, 661-672, 1967.

Goddijn-Murphy, L., Woolf, D. K., and Callaghan, A. H.: Parameterizations and algorithms for oceanic whitecap coverage, J. Phys. Oceanogr., 41, 742-756, 2011.

Gong, S. L.: A parameterization of sea-salt aerosol source function for sub- and super-micron particles, Global Biogeochem. Cycles, 17, 1097, 2003.

Graedel, T. E. and Keene, W. C.: The budget and cycle of Earth‘s natural chlorine, Pure Appl. Chem., 68, 1689-1697, 1996.

Grythe, H., Ström, J., Krejci, R., Quinn, P., and Stohl, A.: A review of sea-spray aerosol source functions using a large global set of sea salt aerosol concentration measurements, Atmos. Chem. Phys., 14, 1277–1297, 2014.

Hanson, J. L., and Phillips, O. M.: Wind sea growth and dissipation in the open ocean, J. Phys. Oceanogr., 29, 1633-1648, 1999.

Jaeglé, L., Quinn, P. K., Bates, T. S., Alexander, B., and Lin, J.-T.: Global distribution of sea salt aerosols: new constraints from in situ and remote sensing observations, Atmos. Chem. Phys., 11, 3137-3157, doi:10.5194/acp-11-3137-2011, 2011.

Kara, A. B., Wallcraft, A. J., and Bourassa, M. A.: Air-sea stability effects on the 10 m winds over the global ocean: Evaluations of air-sea flux algorithms, J. Geophys. Res.-Oceans, 113, C04009, 2008.

Keene, W. C., Pszenny, A. A. P., Jacob, D. J., Duce, R. A., Galloway, J. N., Schultz-Tokos, J. J., Sievering, H., and Boatman, J. F.: The geochemical cycling of reactive chlorine through the marine troposphere, Global Biogeochem. Cy., 4 (NO. 4), 407-430, 1990.

Keene, W. C., Khalil, M. A. K., Erickson, D. J., McCulloch, A., Graedel, T. E., Lobert, J. M., Aucott, M. L., Gong, S.-L., Harper, D. B., Kleiman, G., Midgley, P., Moore, R. M., Seuzaret, C., Sturges, W. T., Benkovitz, C. M., Koropalov, V., Barrie, L. A., and Li, Y.-F.: Composite global emissions of reactive chlorine from anthropogenic and natural sources: reactive chlorine emissions inventory, J. Geophys. Res., 104 (NO. D7), 8429-8440, 1999.

Kleiss, J. M. and Melville, W. K.: The analysis of sea surface imagery for whitecap kinematics, J. Atmos. Ocean. Tech, 28, 219-243, 2011.

Koop, T., Kapilashrami, A., Molina, L.T., and Molina, M. J.: Phase transitions of sea-salt/water mixtures at low temperatures: implications for ozone chemistry in the polar marine boundary layer, J. Geophys. Res., 105 (NO. D21), 26393-26402, 2000.

Leckler, F., Arduin, F., Filipot, J.-F., Mironov, A.: Dissipation source terms and whitecap statistics, Ocean Modell., 70, 62-74, 2013.

Lewis, E. R. and Schwartz, S. E.: Sea salt aerosol production: mechanisms, methods, measurements and models - A critical review, Geoph. Monog. Series, 152, American Geophysical Union, Washington D. C., 413 pp, 2004.

Luria, M. and Sievering, H.: Heterogeneous and homogeneous oxidation of SO_2 in the remote marine atmosphere, Atmos. Environ., 25A, 1489-1496, 1991.

Mårtensson, E. M., Nilsson, E. D., de Leeuw, G., Cohen, L. H., and Hansson, H.–C.: Laboratory simulations and parameterization of the primary marine aerosol production, J. Geophys. Res., 108, 4297, 2003.

Medwin, H.: In situ acoustic measurements of microbubbles at sea, J. Geophys. Res., 82, 971-976, 1977.

Meissner, T. and Wentz, F. J.: The emissivity of the ocean surface between 6 and 90 GHz over a large range of wind speeds and earth incidence angles, IEEE T. Geosci. Remote, 50, 3004-3026, 2012.

Melville, W. K.: The role of surface-wave breaking in air-sea interaction, Annu. Rev. Fluid Mech., 28, 279-321, 1996.

Monahan, E. C.: Oceanic Whitecaps, J. Phys. Oceanogr., 1, 139-144, 1971.

Monahan, E. C. and O'Muircheartaigh, I.: Optimal power-law description of oceanic whitecap coverage dependence on wind speed, J. Phys. Oceanogr., 10, 2094–2099, 1980.

Monahan, E. C. and O'Muircheartaigh, I.: Whitecaps and the passive remote sensing of the ocean surface, Int. J. Remote Sens., 7, 627-642, 1986.

Monahan, E. C. and Woolf, D. K.: Comments on "Variations of whitecap coverage with wind stress and water temperature, J. Phys. Oceanogr., 19, 706–709, 1989.

Monahan, E. C., Fairall, C. W., Davidson, K. L., and Boyle, P. J.: Observed inter-relations between 10 m winds, ocean whitecaps and marine aerosols, Q. J. Roy. Meteor. Soc., 109, 379-392, 1983.

Monahan, E. C., Spiel, D. E., and Davidson, K. L.: A model of marine aerosol generation via whitecaps and wave disruption, in: Oceanic whitecaps: and their role in air-sea exchange

processes, Monahan, E. C., Mac Niocaill, G., D. Reidel Publishing Company, Dordrecht, The Netherlands, 167-174, 1986.

Norris, S. J., Brooks, I. M., Moat, B. I., Yelland, M. J., de Leeuw, G., Pascal, R. W., Brooks, B. J.: Near-surface measurements of sea spray aerosol production over whitecaps in the open ocean. Ocean Science, 9, 133–145, doi: 10.5194/os-9-133-2013, 2013a.

Norris, S. J., Brooks, I. M., and Salisbury, D. J.: A wave roughness Reynolds number parameterization of the sea spray source flux, Geophys. Res. Lett., 40, 4415–4419, 2013b.

O'Dowd, C. D. and de Leeuw, G.: Marine aerosol production: a review of the current knowledge, Philos. T. R. Soc. A, 365, 1753-1774, 2007.

O'Dowd, C. D., Lowe, J. A., Smith, M. H., and Kaye, A. D.: The relative importance of non-sea-salt sulphate and sea-salt aerosol to the marine cloud condensation nuclei population: An improved multi-component aerosol-cloud droplet parametrization, Q. J. Roy. Meteor. Soc., 125, 1295-1313, 1999.

O'Dowd, C. D., Facchini, M. C., Cavalli, F., Ceburnis, D., Mircea, M., Decesari, S., Fuzzi, S., Yoon, Y. J., and Putaud, J.-P.: Biogenically driven organic contribution to marine aerosol, Nature, 431, 676-680, 2004.

Ovadnevaite, J., Manders, A., de Leeuw, G., Ceburnis, D., Monahan, C., Partanen, A .-I., Korhonen, H., and O'Dowd, C. D.: A sea spray aerosol flux parameterization encapsulating wave state, Atmos. Chem. Phys., 14, 1837-1852, 2014.

Paget, A. C., Bourassa, M. A., and Anguelova, M. D.: Comparing in situ and satellite-based parameterizations of oceanic whitecaps, J. Geophys. Res. Oceans, 120, 2826–2843, 2015.

Pandey, P. C. and Kakar, R. K.: An empirical microwave emissivity model for a foam-covered sea, IEEE J. Oceanic Eng., 7, 135-140, 1982.

Partanen, A.-I., Dunne, E. M., Bergman, T., Laakso, A., Kokkola, H., Ovadnevaite, J., Sogacheva, L., Baisnée, D., Sciare, J., Manders, A., O'Dowd, C., de Leeuw, G., and Korhonen, H.: Global modelling of direct and indirect effects of sea spray aerosol using a source function encapsulating wave state, Atmos. Chem. Phys., 14, 11731-11752, 2014.

Quilfen, Y., Prigent, C., Chapron, B., Mouche, A. A., and Houti, N.: The potential of QuikSCAT and WindSat observations for the estimation of sea surface wind vector under severe weather conditions, J. Geophys. Res., 112, C09023, 2007.

Reising, S., Asher, W., Rose, L., and Aziz, M.: Passive polarimetric remote sensing of the ocean surface: The effects of surface roughness and whitecaps, paper presented at the International Union of Radio Science, URSI Gen. Assem., Maastrict, Netherlands, 2002.

Saiz-Lopez, A. and von Glasow, R.: Reactive halogen chemistry in the troposphere, Chem. Soc. Rev., 41, 6448-6472, 2012.

Salisbury, D. J., Anguelova, M. D., and Brooks, I. M.: On the variability of whitecap fraction using satellite-based observations, J. Geophys. Res.-Oceans, 118, 6201-6222, 2013.

Salisbury, D. J., Anguelova, M. D., and Brooks, I. M.: Global distribution and seasonal dependence of satellite-based whitecap fraction, Geophys. Res. Lett., 41, 1616–1623, 2014.

Savelyev, I. B., Anguelova, M. D., Frick, G. M., Dowgiallo, D. J., Hwang, P. A., Caffrey, P. F., and Bobak, J. P.: On direct passive microwave remote sensing of sea spray aerosol production, Atmos. Chem. Phys., 14, 11611-11631, 2014.

Sievering, H., Boatman, J., Gorman, E., Kim, Y., Anderson, L., Ennis, G., Luria, M., and Pandis, S.: Removal of sulphur from the marine boundary layer by ozone oxidation in sea-salt aerosols, Nature, 360, 571-573, 1992.

Sievering, H., Gorman, E., Ley, T., Pszenny, A., Springer-Young, M., Boatman, J., Kim, Y., Nagamoto, C., and Wellman, D.: Ozone oxidation of sulfur in sea-salt aerosol particles during the Azores Marine Aerosol and Gas Exchange experiment, J. Geophys. Res. -Atmos., 100, 23075-23081, 1995.

Smith, M. H., Park, P. M., and Consterdine, I. E.: Marine aerosol concentrations and estimated fluxes over the sea, Q. J. Roy. Meteor. Soc., 119, 809–824, 1993.

Smith, M. H. and Harrison, N. M.: The sea spray generation function, J. Aerosol Sci., 29 (Suppl. 1), S189-S190, 1998.

Sofiev, M., Soares, J., Prank, M., de Leeuw, G., and Kukkonen, J.: A regional-to-global model of emission and transport of sea salt particles in the atmosphere, J. Geophys. Res., 116, D21302, 2011.

Stramska, M. and Petelski, T.: Observations of oceanic whitecaps in the north polar waters of the Atlantic, J. Geophys. Res., 108, NO. C3, 3086, 2003.

Tang, W., Yueh, S. H., Fore, A. G., and Hayashi A.: Validation of Aquarius sea surface salinity with in situ measurements from Argo floats and moored buoys, J. Geophys. Res. Oceans, 119, 6171–6189, 2014, doi:10.1002/2014JC010101.

Textor, C., Schulz, M., Guibert, S., Kinne, S., Balkanski, Y., Bauer, S., Berntsen, T., Berglen, T., Boucher, O., Chin, M., Dentener, F., Diehl, T., Easter, R., Feichter, H., Fillmore, D., Ghan, S., Ginoux, P., Gong, S., Grini, A., Hendricks, J., Horowitz, L., Huang, P., Isaksen, I., Iversen, T., Kloster, S., Koch, D., Kirkevåg, A., Kristjansson, J. E., Krol, M., Lauer, A., Lamarque, J. F., Liu, X., Montanaro, V., Myhre, G., Penner, J., Pitari, G., Reddy, S., Seland, Ø., Stier, P., Takemura, T., and Tie, X.: Analysis and quantification of the diversities of aerosol life cycles within AeroCom, Atmos. Chem. Phys., 6, 1777-1813, 2006.

Toba, Y. and Chaen, M.: Quantitative expression of the breaking of wind waves on the sea surface, Records of Oceanographic Works in Japan, 12 (NO. 1), 1-11, 1973.

Thorpe, S. A.: On the clouds of bubbles formed by breaking wind-waves in deep water, and their role in air-sea gas transfer, Philos. T. R. Soc. S. -A., 304, 155-210, 1982.

Wanninkhof, R., Asher, W. E., Ho, D. T., Sweeney, C., and McGillis, W. R.: Advances in quantifying air-sea gas exchange and environmental forcing, Annual Review of Marine Science, 1, 213-244, 2009.

Wentz, F. J.: A model function for ocean microwave brightness temperatures, J. Geophys. Res., 88, NO. C3, 1892-1908, 1983.

Wentz, F. J.: A well-calibrated ocean algorithm for special sensor microwave / imager, J. Geophys. Res., 102, NO. C4, 8703-8718, 1997.

Woolf, D. K.: Bubbles and their role in gas exchange, in: The Sea Surface and Global Change, Liss, P. S. and Duce, R. A., Cambridge Univ. Press, New York, 173-205, 1997.

Wu, J.: Variations of whitecap coverage with wind stress and water temperature, J. Phys. Oceanogr., 18, 1448-1453, 1988.

Zhao, D. and Toba, Y.: Dependence of whitecap coverage on wind and wind-wave properties, J. Oceanogr., 57, 603-616, 2001.

Table 1. Coordinates, number of data points, range and mean value for wind speed, and range and mean value of SST of selected regions (a) for January 2006, (b) for July 2006.

a

Region	Lon.	Lat.	Number of samples*	Wind speed* [m s^{-1}]			SST* [˚C]		
				Range	Mean	Median	Range	Mean	Median
1.	86°W − 95°W	23°N–28°N	18896	1.3−15.7	7.5	7.6	19.4−26.0	23.8	24.1
2.	1°W − 15°W	1°S – 30°S	169128	0.2−12.9	6.4	6.4	21.4−27.8	24.2	24.1
3.	75° E − 89° E	1°S −30°S	169056	0.0−13.4	7.0	7.2	23.0−29.4	26.8	27.3
4.	11°W − 20°W	30°N – 44°N	49760	0.2−19.6	8.0	7.6	13.3−20.4	16.4	16.3
5.	86°W −100°W	31°S – 60°S	200360	0.5−23.0	8.7	8.7	4.8−24.1	12.7	11.7
6.	171°W −180°W	15°S−14°N	123328	0.6−15.6	8.2	8.2	26.2−30.4	28.4	28.2
7.	31°W − 50°W	10°N – 29°N	90640	0.3−20.0	8.8	9.0	20.1−27.9	24.9	25.3
8.	140°W − 160°W	20°S − 30°S	50040	0.5−16.3	6.8	6.7	22.2−29.1	26.3	26.6
9.	140°W − 160°W	40°S − 50°S	41840	0.1−20.6	6.9	6.5	9.3−18.2	13.2	13.1
10.	0°W − 30°W	40°S − 50°S	133080	0.5−26.4	9.4	9.3	3.2−16.7	9.6	9.3
11.	50° E − 70° E	40°S − 50°S	50784	0.5−21.6	9.6	9.6	3.2−17.4	9.6	9.5
12.	180° E − 180°W	60°S − 90°S	576576	0.2−20.9	7.0	6.7	-1.9−8.0	1.8	1.4

* For January 2006.

1

2 b

Region	Lon.	Lat.	Number of samples**	Wind speed** [m s^{-1}]			SST**[˚C]		
				Range	Mean	Median	Range	Mean	Median
1.	86°W − 95°W	23°N–28°N	13848	0.4−10.0	4.5	4.4	28.7−30.5	29.5	29.4
2.	1°W − 15°W	1°S – 30°S	189600	0.2−14.0	6.6	6.6	17.7−27.1	23.2	23.7
3.	75° E − 89° E	1°S −30°S	195424	0.6−15.4	8.0	8.1	18.8−30.0	25.4	25.9
4.	11°W − 20°W	30°N – 44°N	43040	0.7−14.0	6.7	6.6	16.9−23.3	20.4	20.5
5.	86°W −100°W	31°S – 60°S	257496	0.7−22.7	9.8	9.6	2.5−19.1	9.3	8.3
6.	171°W −180°W	15°S−14°N	133096	0.1−14.8	6.0	6.0	26.9−29.7	28.8	29.0
7.	31°W − 50°W	10°N – 29°N	88304	0.4−13.6	7.4	7.4	23.6−28.0	26.0	26.1
8.	140°W − 160°W	20°S − 30°S	47504	0.7−24.7	6.9	6.2	18.8−27.0	23.2	23.4
9.	140°W − 160°W	40°S − 50°S	52736	0.5−21.0	10.1	10.3	8.2−14.1	10.9	10.8
10.	0°W − 30°W	40°S − 50°S	160192	0.9−28.9	10.8	10.8	1.8−14.6	8.3	8.3
11.	50° E − 70° E	40°S − 50°S	49344	1.1−28.2	12.9	12.7	2.1−16.1	8.3	7.8
12.	180° E − 180°W	60°S − 90°S	177240	0.8−29.1	11.7	11.9	-1.3−4.3	1.7	1.7

3 ** For July 2006

4

Figure captions

Figure 1. Satellite retrieved 37 GHz W data for 11 March 2006. a) Map (0.5°×0.5°) of ascending and descending passes for W at 37 GHz; b) W at 10 and 37 GHz (green and magenta symbols, respectively) compared to historical photographic data including total W (diamonds) and active whitecap fraction W_A (squares). Parameterization $W(U_{10})$ of Monahan and O'Muircheartaigh (1980, MOM80) (purple line) is shown for reference.

Figure 2. Selected regions to determine regional variations of $W(U_{10})$.

Figure 3. Seasonal cycle for 2006 in different regions as defined in Fig. 2 and Table 1: a) wind speed U_{10}; b) Sea surface temperature (SST) T. The regions represent: 4–Temperate zone in Northern hemisphere; 5–Temperate zone in Southern hemisphere; 6–Doldrums along the Equator; 12–Lowest SST.

Figure 4. Scatter plot for March 2006 of (a) global $U_{10\mathrm{ECMWF}}$ versus $U_{10\mathrm{QSCAT}}$ and (b) global T from ECMWF versus T from GDAS. In both figures the colors indicate the amount of data points per hexabin. The black lines are linear fits: the dashed line represents unrestricted fit and the solid line a fit forced through zero. The linear regressions and respective R^2 are listed in each panel.

Figure 5. Global W as function of U_{10} from QuikSCAT for March 2006 where W is obtained with 10 GHz (a) and 37 GHz (b) measurement frequency. The red line indicates the Monahan and O'Muircheartaigh (1980 MOM80) relationship (Eq. (3)). The colors indicate the amount of data points per hexabin.

Figure 6. Global $\sqrt{W}$ as function of U_{10} from QuikSCAT for March 2006, where $\sqrt{W}$ is obtained with 10 GHz (a) and 37 GHz (b) measurement frequency. The black line (in both panels) indicates the best linear fit through the data. The red line in Fig. 6b equals the black line in Fig. 6a. The colors indicate the amount of data points per hexabin.

Figure 7. Scatter plot of $\sqrt{W}$ versus $U_{10\mathrm{ECMWF}}$ for March 2006.

Figure 8. Linear fits of $\sqrt{W}$ versus U_{10} for: region 1 for January 2006 at 10 GHz (a) and 37 GHz (b); region 5 for all months at 10 GHz (c) and 37 GHz (d); regions 1-12 for March 2006 at 10 GHz (e) and 37 GHz (f).

Figure 9. Seasonal cycle for 2006 of regression coefficients in the $\sqrt{W}(U_{10})$ linear fits for different regions as defined in Fig. 2 and Table 1: a) slope m; b) y-intercept c.. The regions represent: 4–Temperate zone in Northern hemisphere; 5–Temperate zone in Southern hemisphere; 6–Doldrums along the Equator; 12–Lowest SST.

Figure 10. Regional and seasonal variations: a) Regionally averaged b values for each month with error bars (± one standard deviation) representing the regional variability; b) Annually averaged b values for each region with error bars representing the seasonal variability.

Figure 11. Sea surface temperature dependences of a) coefficient a (slope) and b) coefficient b (intercept) in the $W(U_{10})$ dependence. Each point is annual mean for different region. The error bars indicate ± 1 standard deviation for SST (horizontal bars) and coefficients (vertical bars). Panel c) shows the monthly means of coefficients b for each region that form one data point in panel b). Regions in Northern hemisphere (NH) are show with squares; regions in Southern hemisphere (SH) are shown with circles. The diamonds are for region 6 at the Equator.

Figure 12. a) Comparison of the new global $W(U_{10})$ parameterization (based on the global W data set) to parameterizations from different studies: SAL13 (10 GHz) and SAL13 (37 GHz) are parameterizations from Salisbury et al. (2013) (Eq. (1)), CAL08 are parameterizations derived by Callaghan et al. (2008) (Eq. (2)); and MOM80 is the parameterization of Monahan and O'Muircheartaigh (1980) (Eq. (3)).

b) Comparison of the new quadratic parameterization $W(U_{10}, T)$ (Eqs. 13-14) at three fixed SST values (T = 20 °C, red line; T = 12 °C, green line; T = 2 °C, blue line) to the global quadratic parameterization $W(U_{10})$ (Eq. 11, black solid line) and the parameterizations of Salisbury et al. (2013) (Eq. (1)) for 10 GHz (dash-dotted line) and 37 GHz (dashed line).

c) Comparison of the new $W(U_{10}, T)$ parameterizations with quadratic (Eqs. 13-14, purple line) and cubic (red line) wind speed exponents at T = 20 °C to the parameterizations of Salisbury et al. (2013, SAL13) (Eq. (1)) for 37 GHz (dashed line) and Monahan and O'Muircheartaigh (1980, MOM80) (blue solid line).

Figure 13. a) As Fig. 1b with W values added from $W(U_{10})$ for 10 and 37 GHz (black lines, Eqs. (10-11)) and $W(U_{10}, T)$ for 10 (red) and 37 GHz (cyan, Eqs. (13-14)). Wind speed and sea surface temperature from the whitecap database are used for the calculations.

b) Difference map of annual average W distribution for 2006 calculated from the Monahan and O'Muircheartaigh (1980, MOM80) $W(U_{10})$ parameterization (Eq. (3)) minus $W(U_{10}, T)$ from Eqs. (13-14) The calculations use wind speed U_{10} is from QuikSCAT in the whitecap database.

Figure 14. a) Annual average super-micron mass emission rate for 2006 in μg m^{-2} s^{-1} calculated from from Eq. (4′)). b) Difference map between the annual average super-micron SSA mass emission rate calculated from the Monahan et al. (1986) SSSF and the annual average super-micron SSA mass emission rate calculated from the Monahan et al. (1986) SSSF where W is replaced with Eqs. (13-14). The calculations use wind speed U_{10} is e from QuikSCAT in the whitecap database.

FIGURES

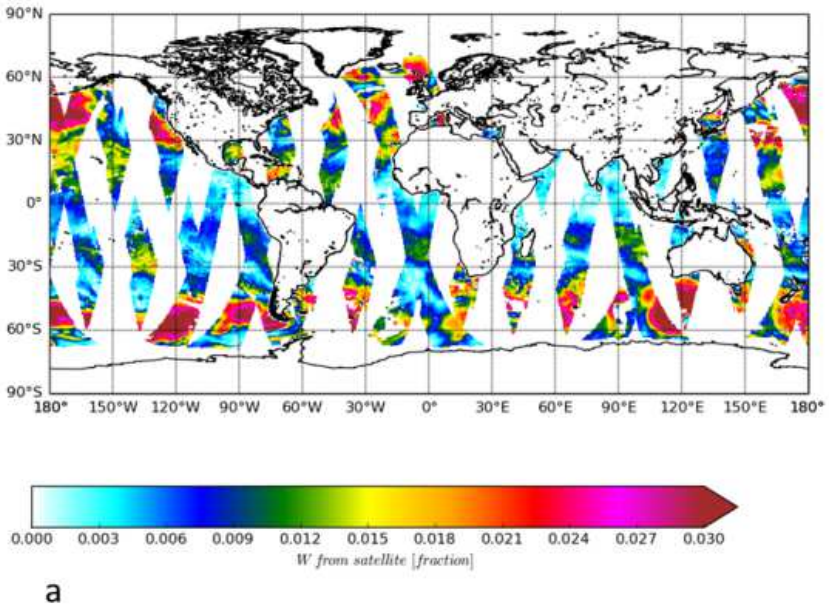

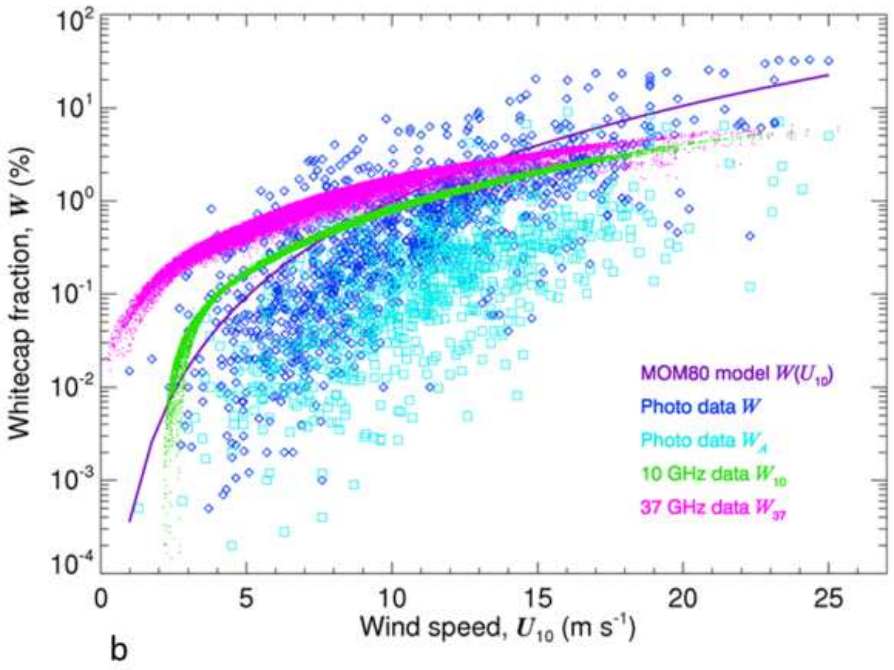

Figure 1

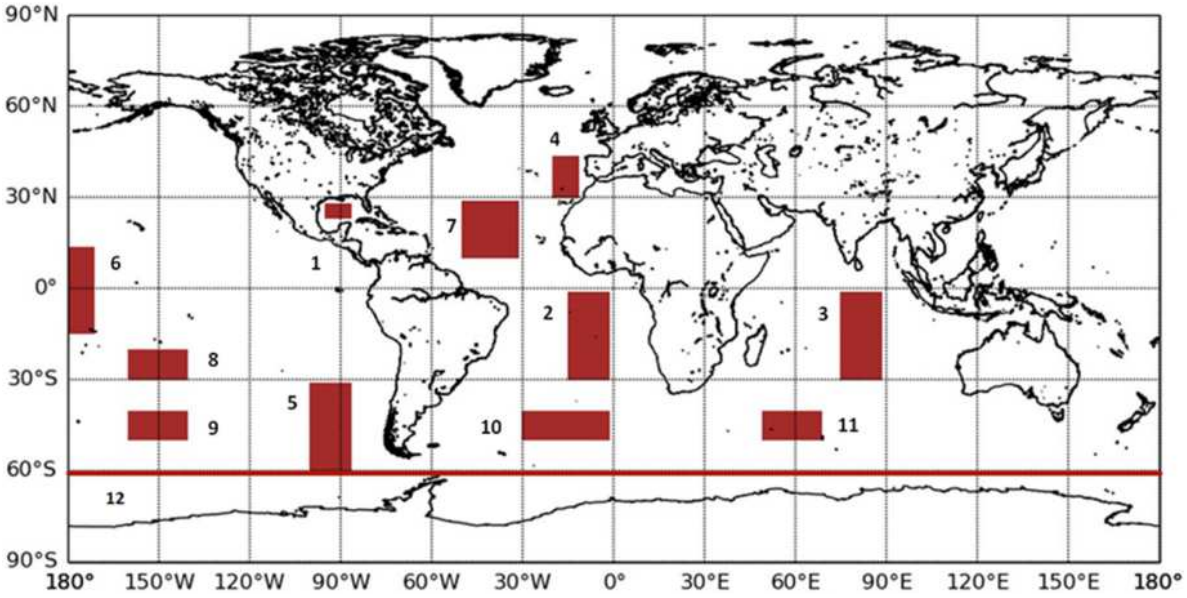
90°N
60°N
30°N
0°
30°S
60°S
90°S
180°
150°W
120°W
90°W
60°W
30°W
0°
30°E
60°E
90°E
120°E
150°E
180°
1
2
3
4
5
6
7
8
9
10
11
12

Figure 2

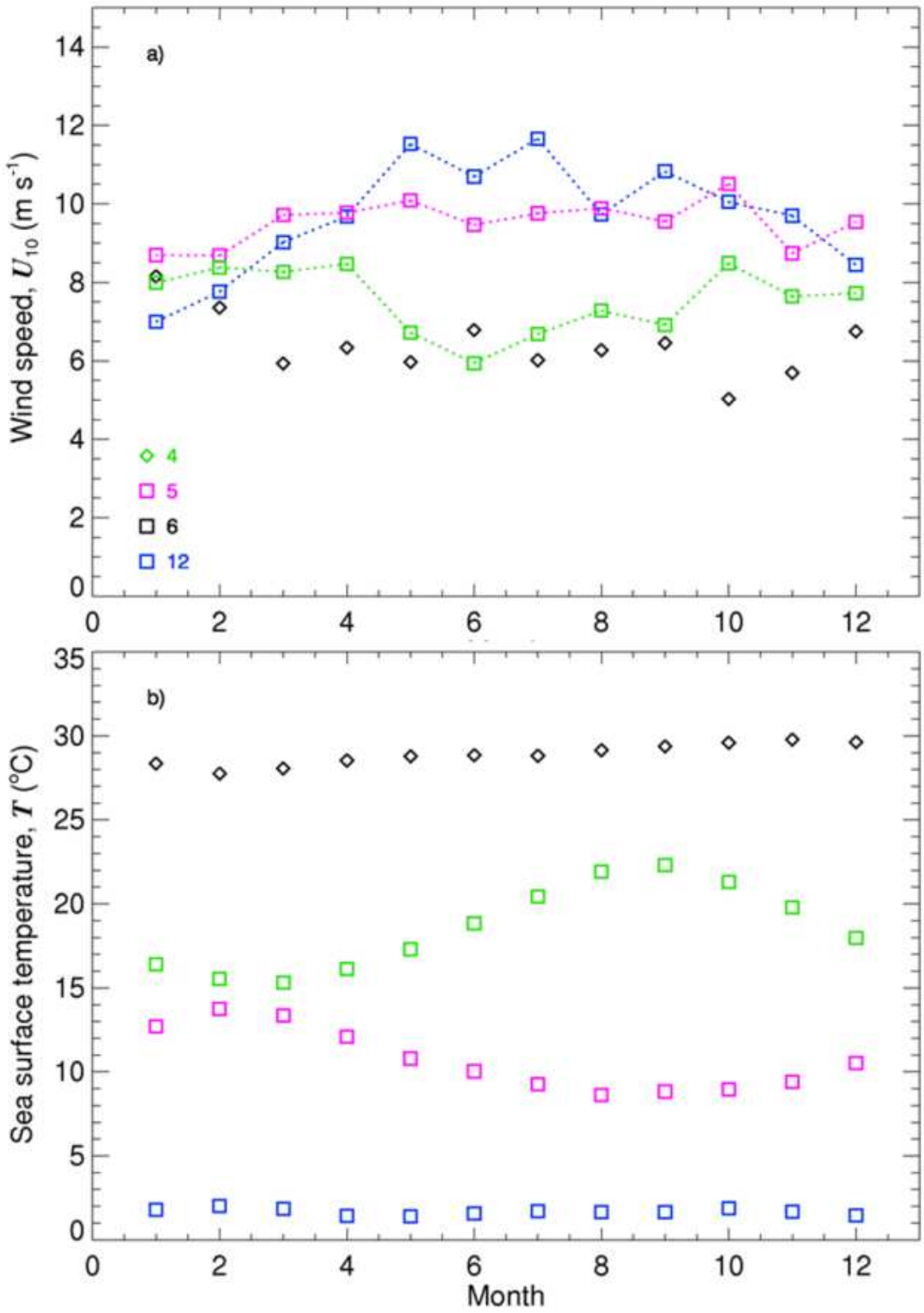
a)
Wind speed, U_{10} (m s^{-1})
4
5
6
12
b)
Sea surface temperature, T (°C)
Month

Figure 3

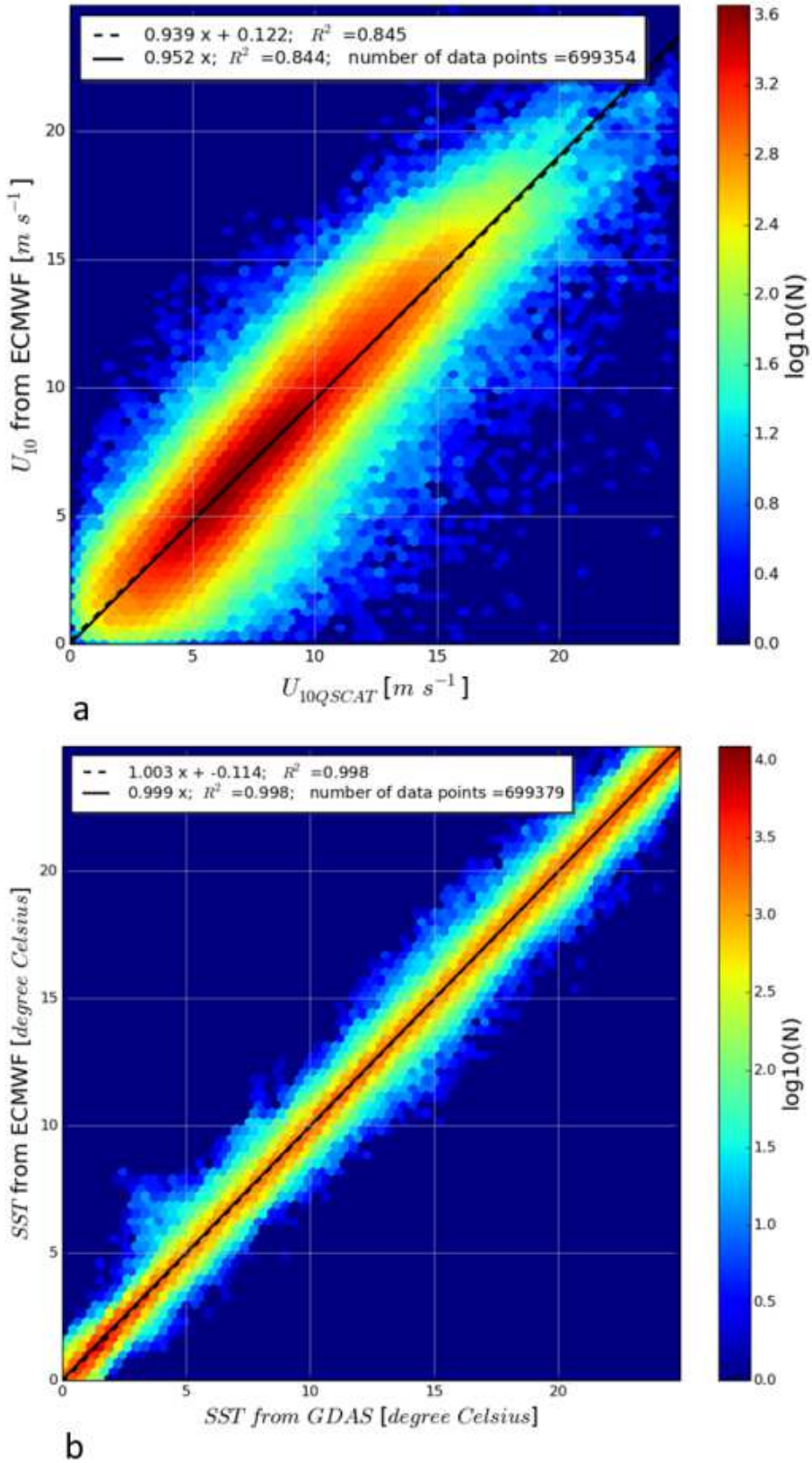
0.939 x + 0.122; R^2 =0.845
0.952 x; R^2 =0.844; number of data points =699354
U_{10} from ECMWF [$m\ s^{-1}$]
$U_{10QSCAT}$ [$m\ s^{-1}$]
log10(N)
a
1.003 x + -0.114; R^2 =0.998
0.999 x; R^2 =0.998; number of data points =699379
SST from ECMWF [degree Celsius]
SST from GDAS [degree Celsius]
log10(N)
b

Figure 4

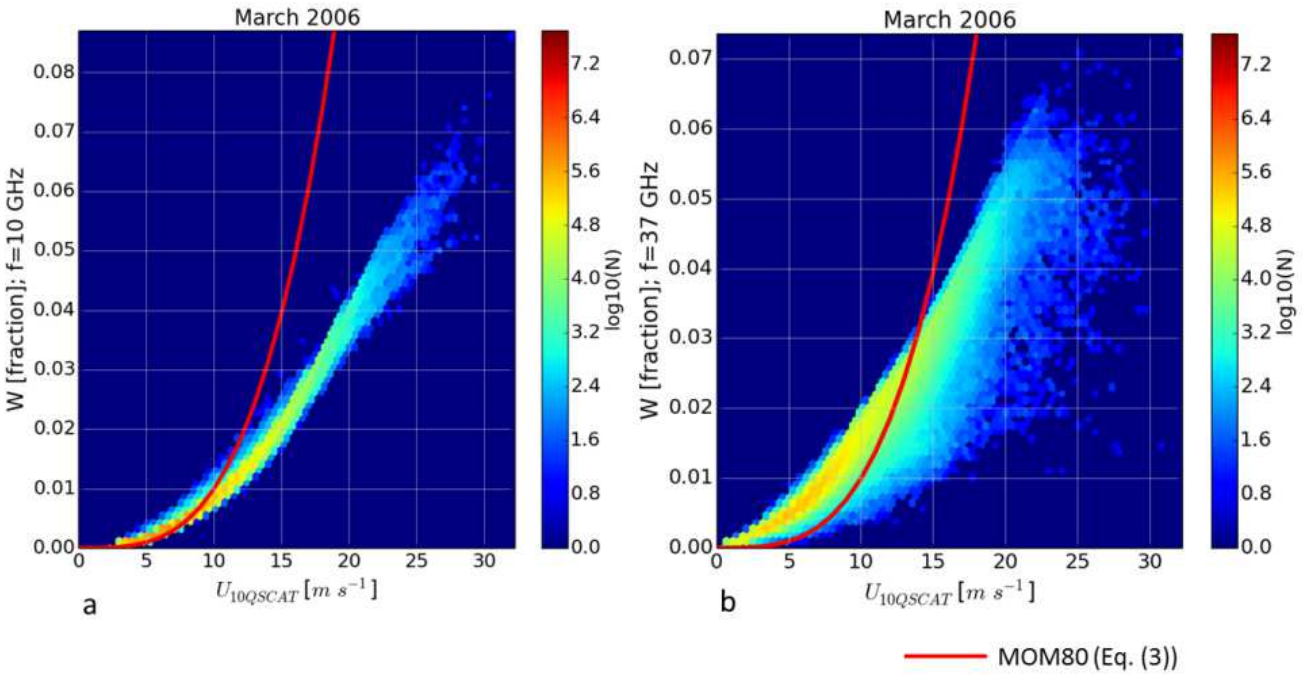
March 2006
W [fraction]; f=10 GHz
$U_{10QSCAT}$ [$m\ s^{-1}$]
log10(N)
a
March 2006
W [fraction]; f=37 GHz
$U_{10QSCAT}$ [$m\ s^{-1}$]
log10(N)
b
MOM80 (Eq. (3))

1

2 Figure 5

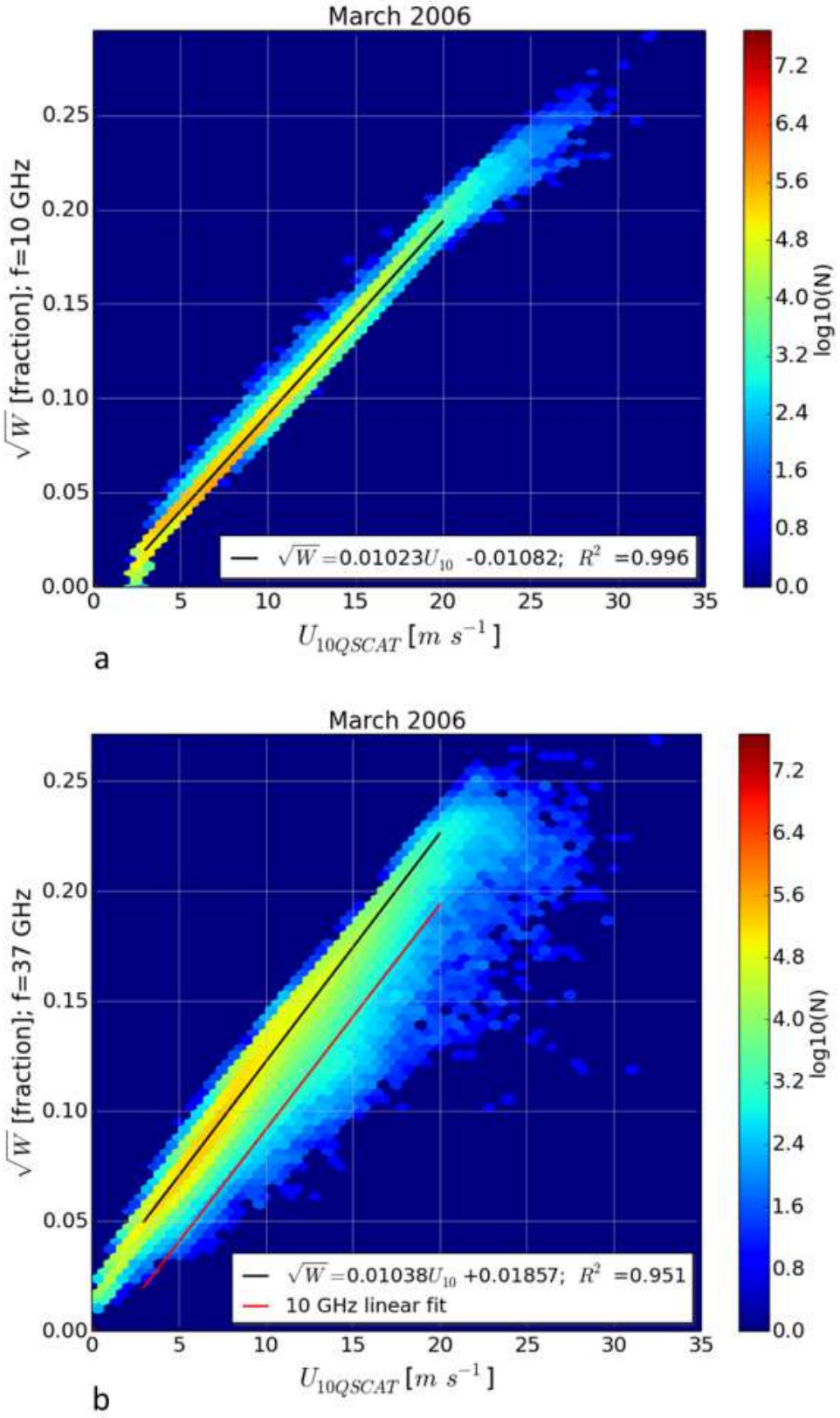
March 2006
$\sqrt{W}$ [fraction]; f=10 GHz
$U_{10QSCAT}$ [$m\ s^{-1}$]
$\sqrt{W}$ =0.01023U_{10} -0.01082; R^2 =0.996
log10(N)
a
March 2006
$\sqrt{W}$ [fraction]; f=37 GHz
$U_{10QSCAT}$ [$m\ s^{-1}$]
$\sqrt{W}$ =0.01038U_{10} +0.01857; R^2 =0.951
10 GHz linear fit
log10(N)
b

1

2 Figure 6

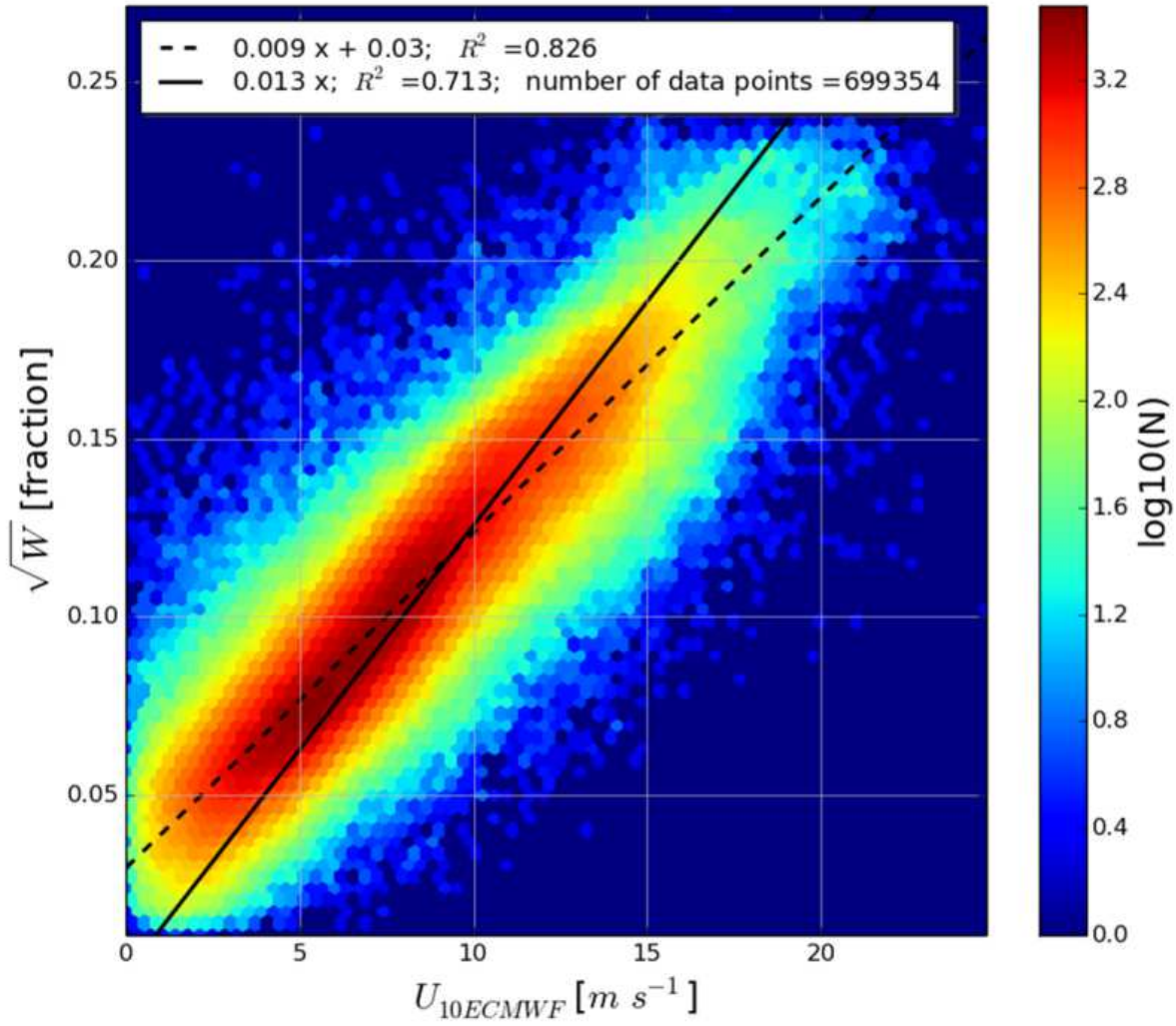
0.009 x + 0.03; R^2 =0.826
0.013 x; R^2 =0.713; number of data points =699354
$\sqrt{W}$ [fraction]
$U_{10ECMWF}$ [$m\ s^{-1}$]
log10(N)
0.25
0.20
0.15
0.10
0.05
0
5
10
15
20
3.2
2.8
2.4
2.0
1.6
1.2
0.8
0.4
0.0

Figure 7

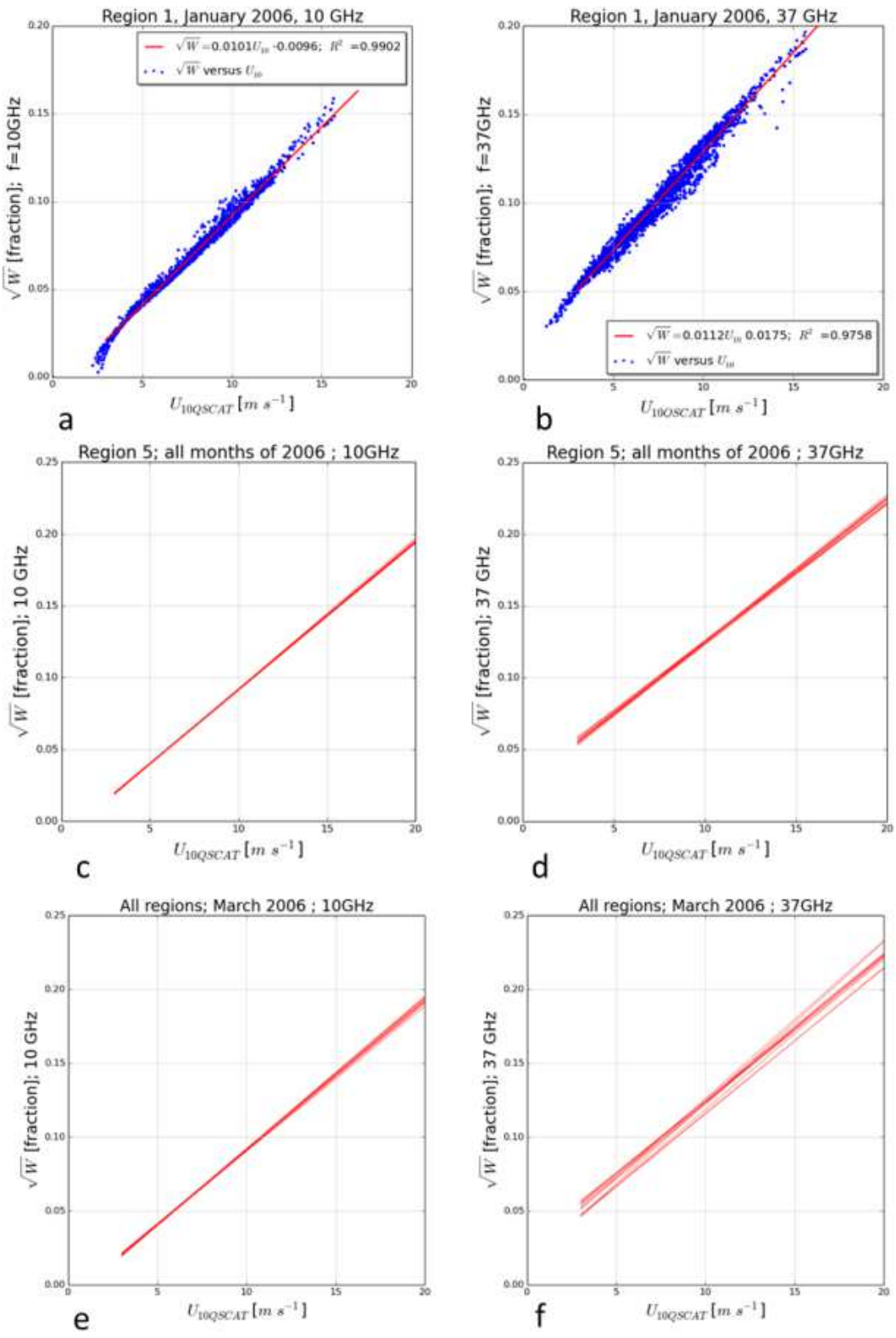
Region 1, January 2006, 10 GHz
$\sqrt{W}$ =0.0101U_{10} -0.0096; R^2 =0.9902
$\sqrt{W}$ versus U_{10}
$\sqrt{W}$ [fraction]; f=10GHz
$U_{10QSCAT}$ [$m\ s^{-1}$]
a
Region 1, January 2006, 37 GHz
$\sqrt{W}$ =0.0112U_{10} 0.0175; R^2 =0.9758
$\sqrt{W}$ versus U_{10}
$\sqrt{W}$ [fraction]; f=37GHz
$U_{10QSCAT}$ [$m\ s^{-1}$]
b
Region 5; all months of 2006 ; 10GHz
$\sqrt{W}$ [fraction]; 10 GHz
$U_{10QSCAT}$ [$m\ s^{-1}$]
c
Region 5; all months of 2006 ; 37GHz
$\sqrt{W}$ [fraction]; 37 GHz
$U_{10QSCAT}$ [$m\ s^{-1}$]
d
All regions; March 2006 ; 10GHz
$\sqrt{W}$ [fraction]; 10 GHz
$U_{10QSCAT}$ [$m\ s^{-1}$]
e
All regions; March 2006 ; 37GHz
$\sqrt{W}$ [fraction]; 37 GHz
$U_{10QSCAT}$ [$m\ s^{-1}$]
f

1

2 Figure 8

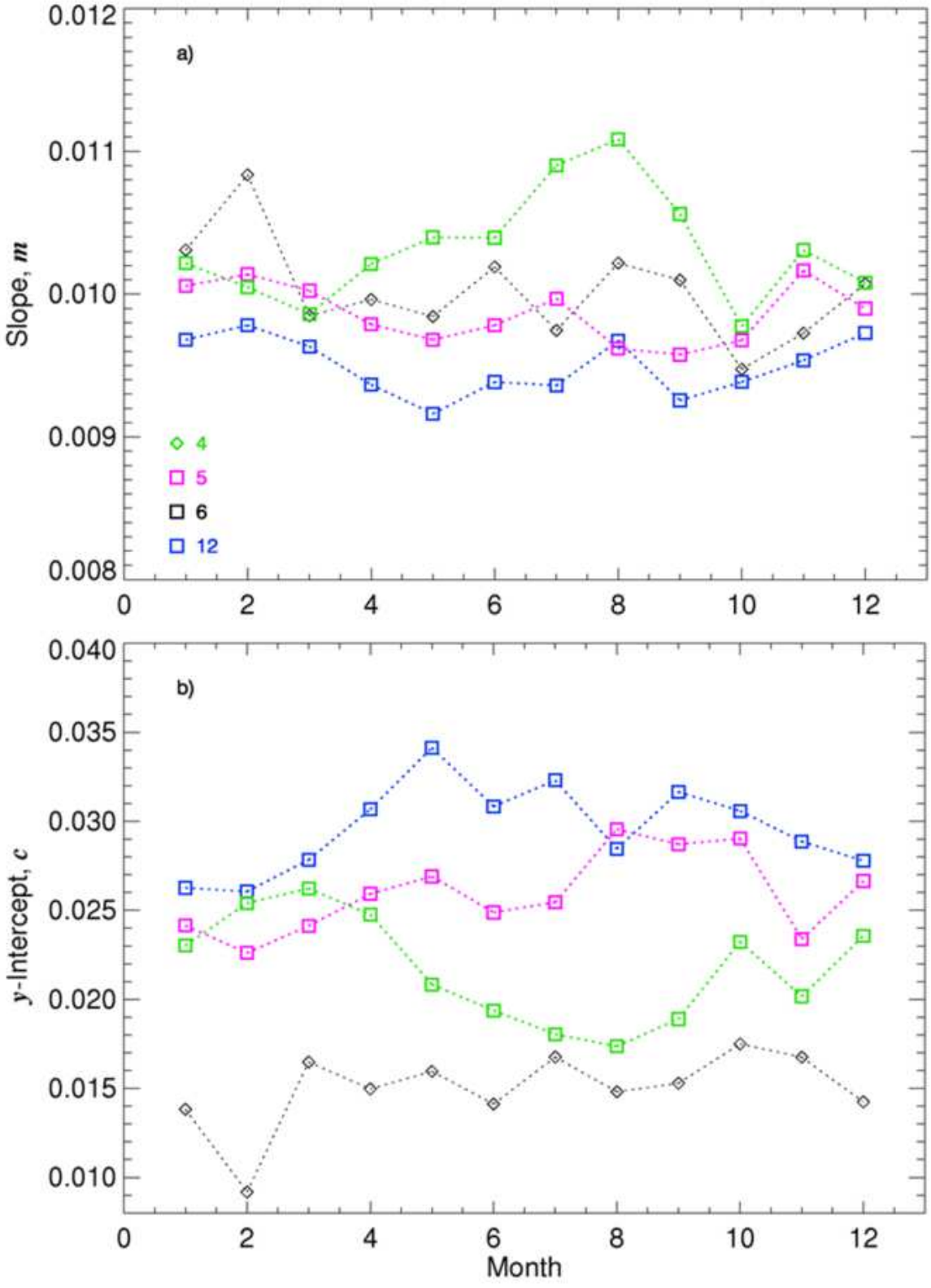
a)
Slope, m
0.012
0.011
0.010
0.009
0.008
4
5
6
12
0
2
4
6
8
10
12
b)
y-Intercept, c
0.040
0.035
0.030
0.025
0.020
0.015
0.010
Month

1
2
3 Figure 9

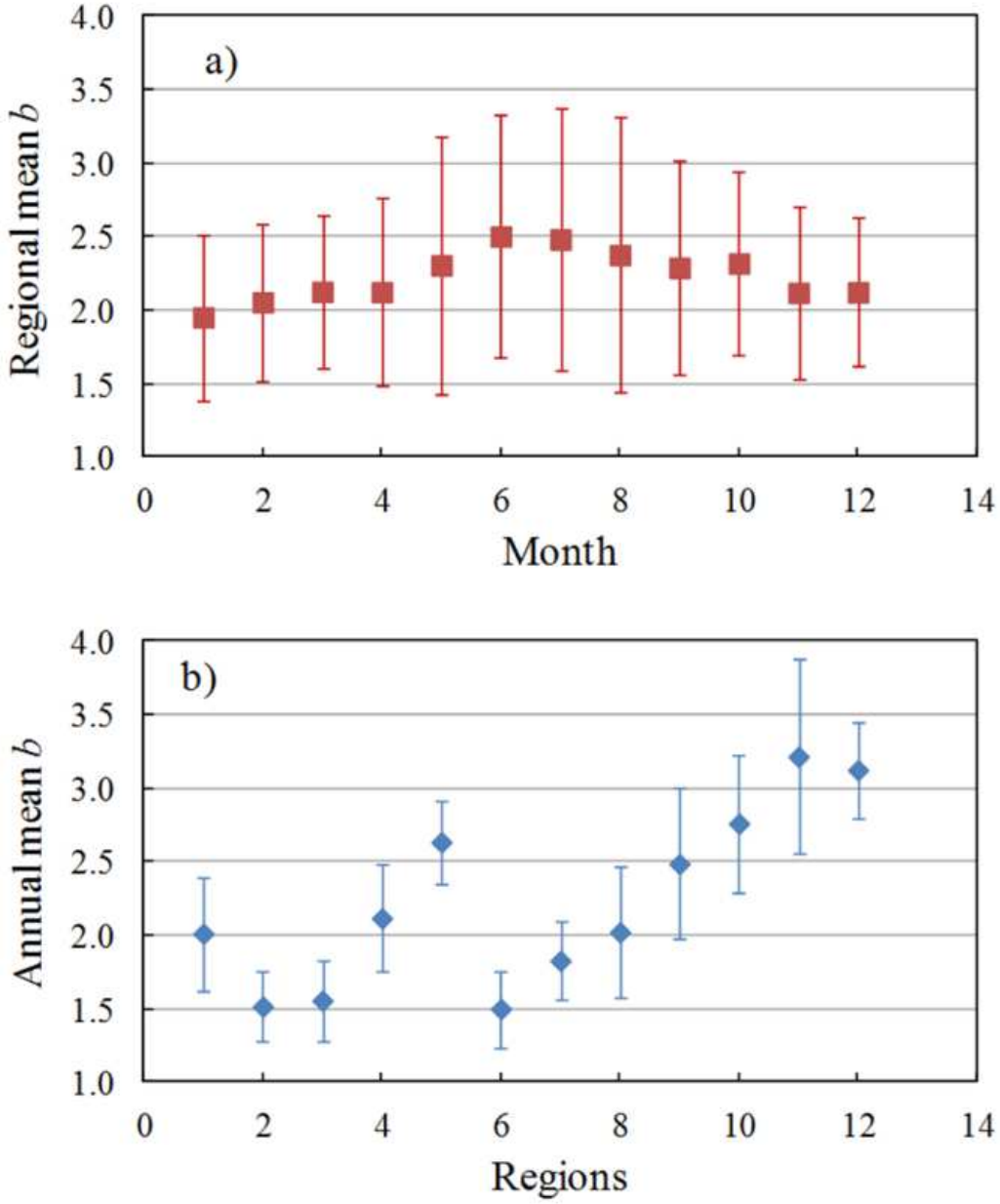
a)
Regional mean b
4.0
3.5
3.0
2.5
2.0
1.5
1.0
0
2
4
6
8
10
12
14
Month
b)
Annual mean b
4.0
3.5
3.0
2.5
2.0
1.5
1.0
0
2
4
6
8
10
12
14
Regions

Figure 10

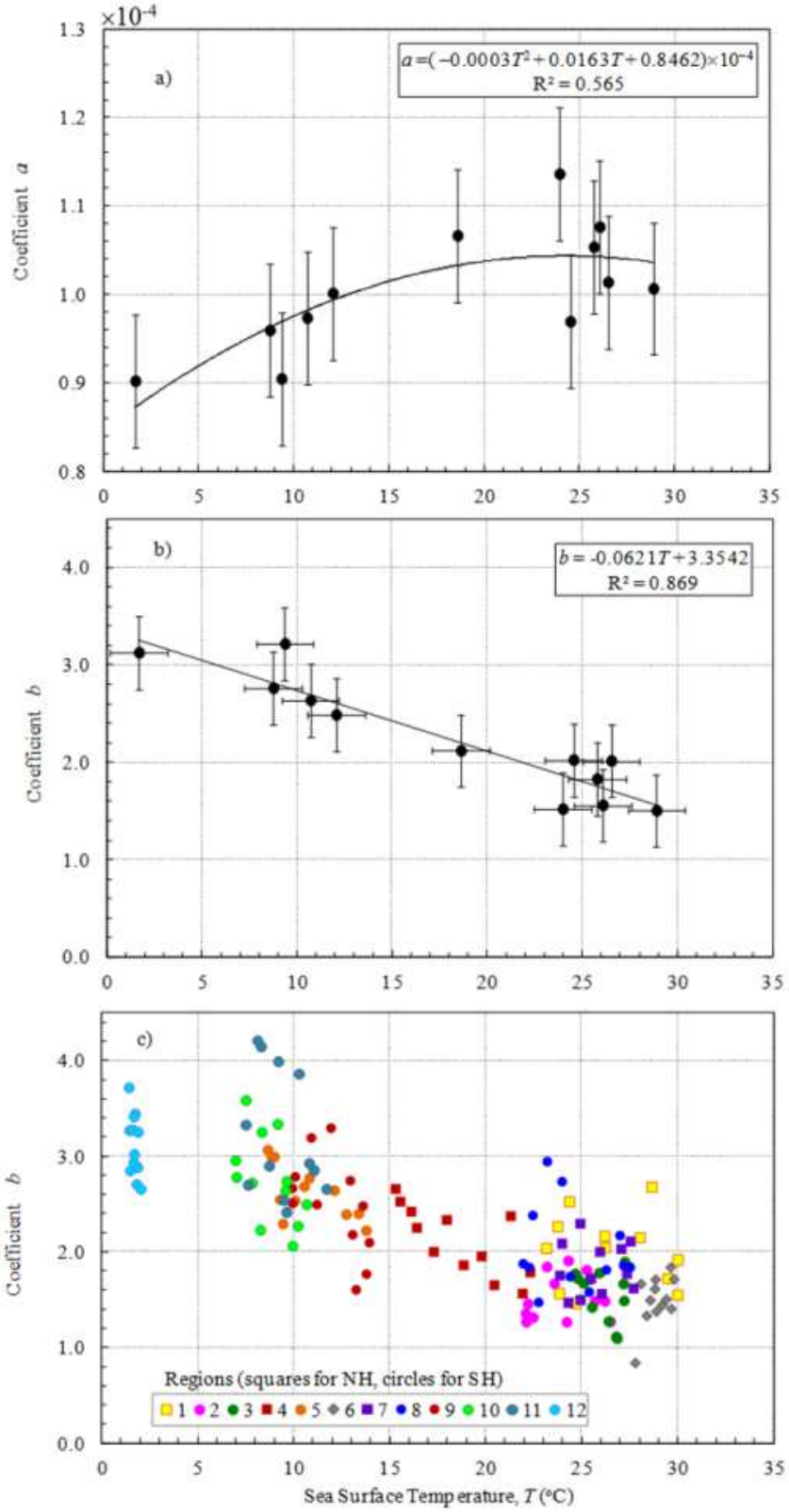
×10⁻⁴
a)
a = (−0.0003T² + 0.0163T + 0.8462)×10⁻⁴
R² = 0.565
Coefficient a
b)
b = -0.0621T + 3.3542
R² = 0.869
Coefficient b
c)
Coefficient b
Regions (squares for NH, circles for SH)
1 2 3 4 5 6 7 8 9 10 11 12
Sea Surface Temperature, T (°C)

Figure 11

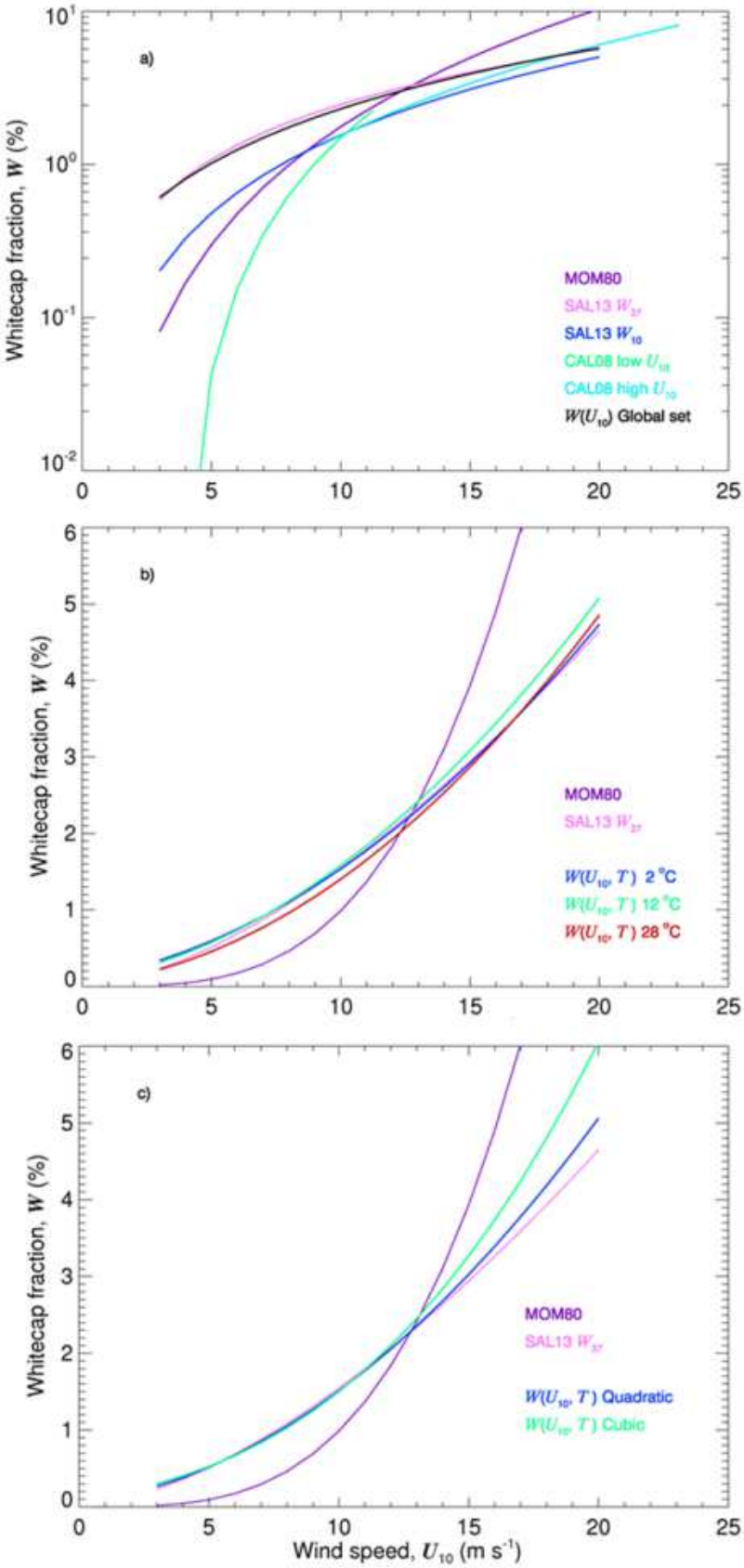
a)
Whitecap fraction, W (%)
MOM80
SAL13 W37
SAL13 W10
CAL08 low U10
CAL08 high U10
W(U10) Global set
b)
Whitecap fraction, W (%)
MOM80
SAL13 W37
W(U10, T) 2 °C
W(U10, T) 12 °C
W(U10, T) 28 °C
c)
Whitecap fraction, W (%)
MOM80
SAL13 W37
W(U10, T) Quadratic
W(U10, T) Cubic
Wind speed, U10 (m s-1)

Figure 12

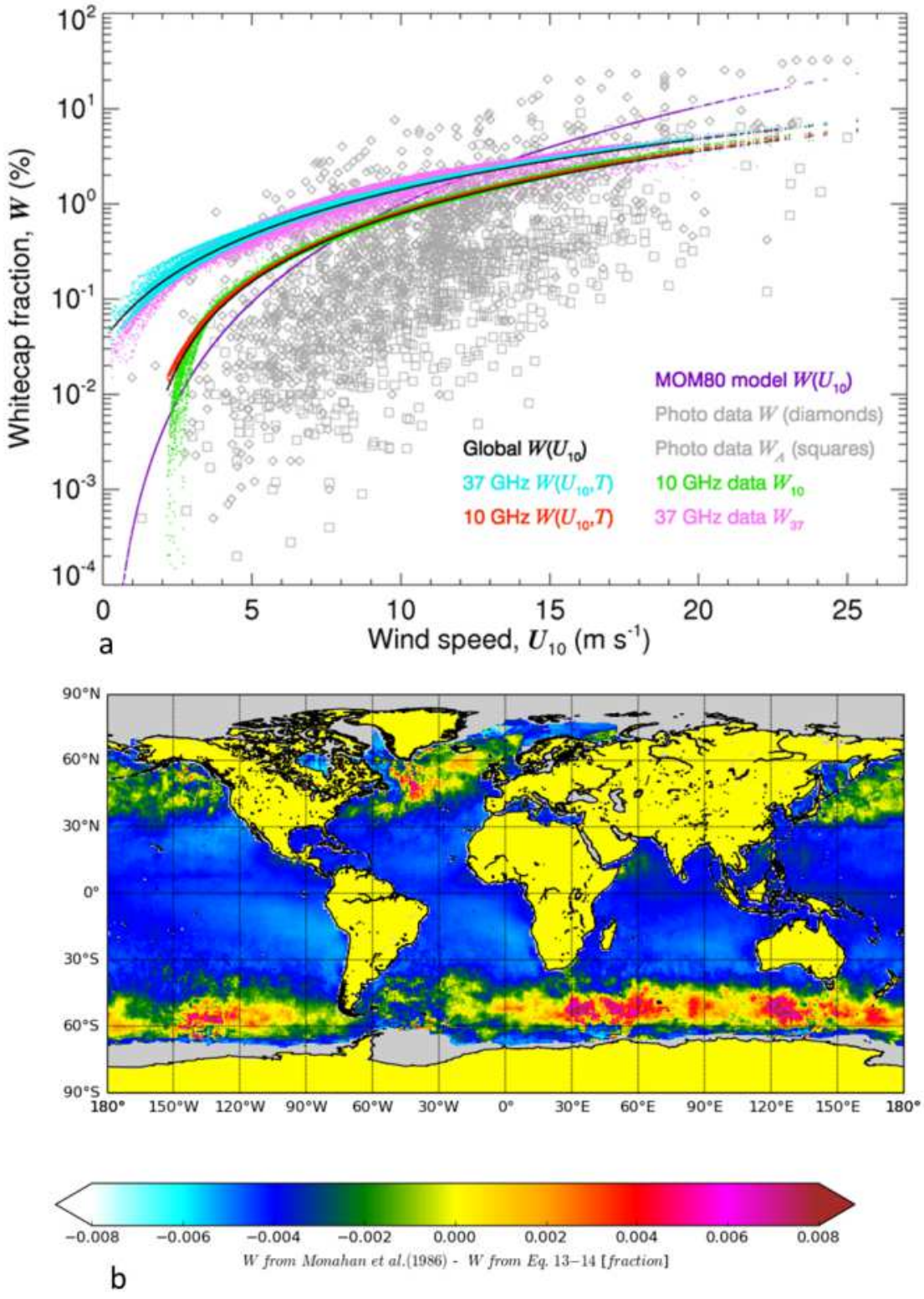
Whitecap fraction, W (%)
Wind speed, U_{10} (m s^{-1})
a
MOM80 model $W(U_{10})$
Photo data W (diamonds)
Photo data W_A (squares)
Global $W(U_{10})$
37 GHz $W(U_{10},T)$
10 GHz $W(U_{10},T)$
10 GHz data W_{10}
37 GHz data W_{37}
90°N
60°N
30°N
0°
30°S
60°S
90°S
180° 150°W 120°W 90°W 60°W 30°W 0° 30°E 60°E 90°E 120°E 150°E 180°
−0.008 −0.006 −0.004 −0.002 0.000 0.002 0.004 0.006 0.008
W from Monahan et al.(1986) - W from Eq. 13–14 [fraction]
b

Figure 13

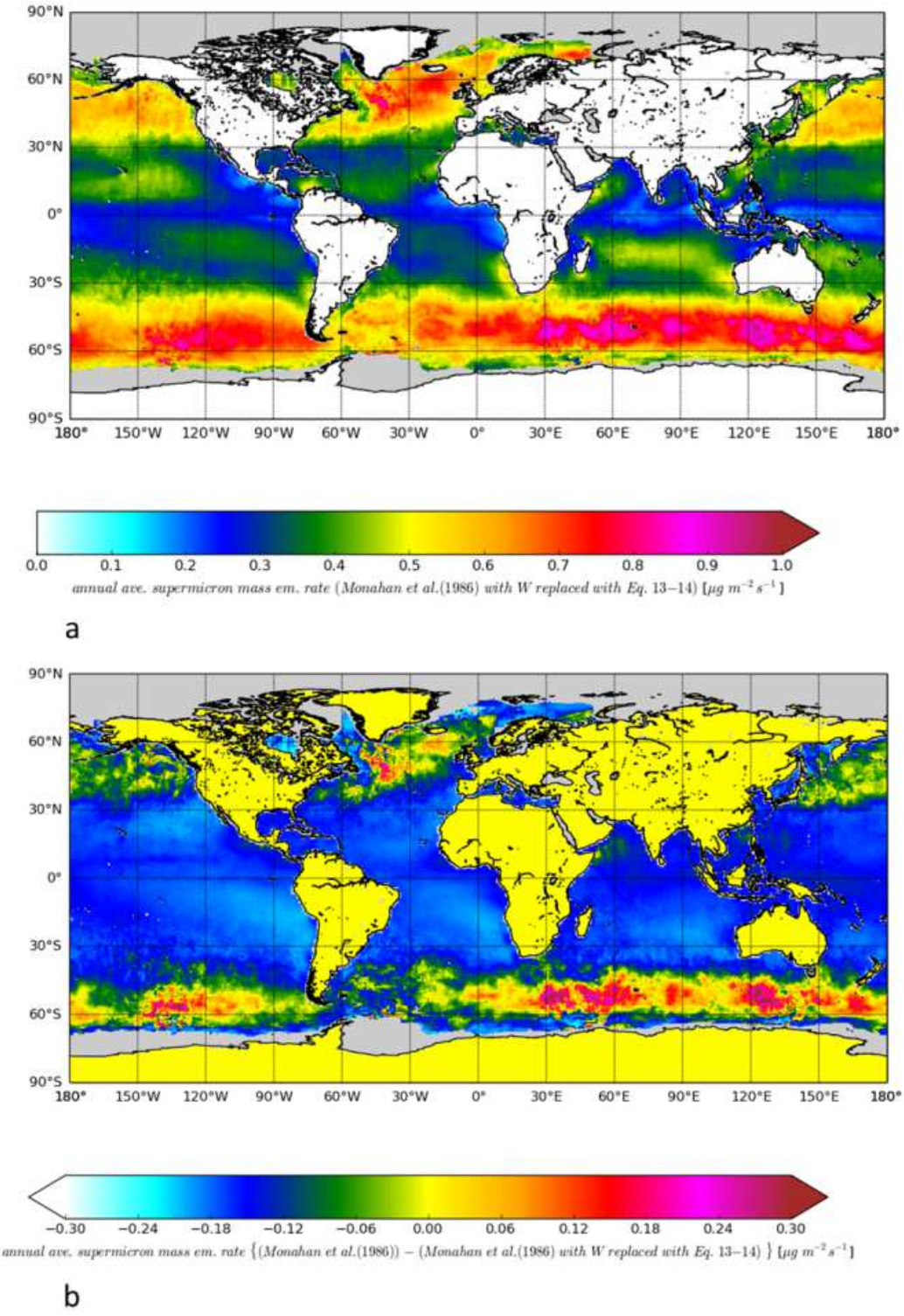
90°N
60°N
30°N
0°
30°S
60°S
90°S
180° 150°W 120°W 90°W 60°W 30°W 0° 30°E 60°E 90°E 120°E 150°E 180°
0.0 0.1 0.2 0.3 0.4 0.5 0.6 0.7 0.8 0.9 1.0
annual ave. supermicron mass em. rate (Monahan et al.(1986) with W replaced with Eq. 13–14) [μg m⁻² s⁻¹]
a
−0.30 −0.24 −0.18 −0.12 −0.06 0.00 0.06 0.12 0.18 0.24 0.30
annual ave. supermicron mass em. rate {(Monahan et al.(1986)) − (Monahan et al.(1986) with W replaced with Eq. 13–14)} [μg m⁻² s⁻¹]
b

Figure 14